

1 **MESMO 3: Flexible phytoplankton stoichiometry and refractory DOM**

2

3 **Katsumi Matsumoto, Tatsuro Tanioka⁺, and Jacob Zahn**

4

5 Department of Earth & Environmental Sciences, University of Minnesota, Minneapolis,
6 Minnesota, USA

7 ⁺ Current affiliation: Department of Earth System Science, University of California Irvine,
8 Irvine, California, USA

9

10 Contact: katsumi@umn.edu

11

12 (revised version submitted 3/18/2021 to *Geoscientific Model Development*)

13

14 **Abstract**

15 We describe the third version of Minnesota Earth System Model for Ocean biogeochemistry
16 (MESMO 3), an earth system model of intermediate complexity, with a dynamical ocean, a
17 dynamic-thermodynamic sea ice, and an energy moisture balanced atmosphere. A major
18 feature of Version 3 is the flexible C:N:P ratio for the three phytoplankton functional types
19 represented in the model. The flexible stoichiometry is based on the power law formulation
20 with environmental dependence on phosphate, nitrate, temperature, and light. Other new
21 features include nitrogen fixation, water column denitrification, oxygen and temperature-
22 dependent organic matter remineralization, and CaCO₃ production based on the concept of
23 the residual nitrate potential growth. Also, we describe the semi-labile and refractory
24 dissolved organic pools of C, N, P, and Fe that can be enabled in MEMSO 3 as an optional
25 feature. The refractory dissolved organic matter can be degraded by photodegradation at
26 the surface and hydrothermal vent degradation at the bottom. These improvements
27 provide a basis for using MESMO 3 in further investigations of the global marine carbon
28 cycle to changes in the environmental conditions of the past, present, and future.

29

30 **1. Introduction**

31 Here we document the development of the third version of the Minnesota Earth System
32 Model for Ocean biogeochemistry (MESMO 3). As described for the first two versions
33 (Matsumoto et al., 2008, 2013), MESMO is based on the non-modular version of the Grid
34 ENabled Integrated Earth (GENIE) system model (Lenton et al., 2006; Ridgwell et al., 2007).
35 The computationally efficient ocean-climate model of Edwards and Marsh (Edwards and
36 Marsh, 2005) forms the core of GENIE's physical model. MESMO is an earth system model
37 of intermediate complexity (EMIC), which occupies a midpoint in the continuum of climate
38 models that span high resolution, comprehensive coupled models on one end and box
39 models at the other end (Claussen et al., 2002). MESMO has a 3D dynamical ocean model on
40 a 36 x 36 equal-area horizontal grid with 10° increments in longitude and uniform in the
41 sine of latitude. There are 16 vertical levels. It is coupled to a 2D energy moisture balanced
42 model of the atmosphere and a 2D dynamic and thermodynamic model of sea ice. Thus,
43 MESMO retains important dynamics, which allow for simulations of transient climate
44 change, while still being computationally efficient.

45
46 Since the first version, MESMO has continued to be developed chiefly for investigations of
47 ocean biogeochemistry (Table 1). Briefly, in MESMO 1, the main improvements over the
48 predecessor GENIE focused on the biological production and remineralization as well as on
49 the uptake of natural radiocarbon (^{14}C) and anthropogenic transient tracers (Matsumoto et
50 al., 2008). The net primary production (NPP) in MESMO 1 occurred in the top two vertical
51 levels representing the surface 100 m and depended on temperature, nutrients, light, and
52 mixed layer depth (MLD). The nutrient dependence was based on the Michaelis-Menten
53 uptake kinetics of phosphate (PO_4), nitrate (NO_3), and aqueous CO_2 . The limiting nutrient
54 was determined by the Liebig's rule of the minimum relative to the fixed uptake
55 stoichiometry of C:N:P=117:16:1. A single generic phytoplankton functional type (PFT)
56 carried out NPP, which was split between particulate organic matter (POM) and dissolved
57 organic matter (DOM) in a globally constant ratio of 1:2. The semi-labile form of the
58 dissolved organic carbon (DOC) was the only form of DOM simulated in MESMO 1. The POM
59 flux across the 100 m level defined the export production. The vertical flux of POM was

60 driven by a fixed rate of sinking and a temperature-dependent, variable remineralization
61 rate.

62

63 The main aim of MESMO 2 was a credible representation of the marine silica cycle
64 (Matsumoto et al., 2013). To this end, the set of limiting nutrients (P, N, and C) in MESMO 1
65 was augmented to include iron (Fe) and silicic acid (Si(OH)_4) in MESMO 2 (Table 1). The
66 stable isotope of Si (^{30}Si) was also added as a state variable. The Fe cycle included an
67 aeolian flux of Fe, complexation with organic ligand, and particle scavenging of free Fe. The
68 scavenged Fe that reached the seafloor was removed from the model domain. This burial
69 flux of Fe balanced the aeolian flux at steady state. Also, a new PFT was added in MESMO 2
70 to represent [chiefly](#) diatoms. This new "large" PFT was limited by Si and characterized by a
71 high maximum growth rate and large half-saturation constants for the nutrient uptake
72 kinetics. It represented fast and opportunistic phytoplankton that do well under nutrient
73 replete conditions. In comparison, the "small" PFT was characterized with a lower
74 maximum growth rate and smaller half-saturation constants and outperformed the large
75 PFT in oligotrophic subtropical gyres. CaCO_3 production was associated with the "small"
76 PFT in MESMO2. The addition of Fe, Si, and the large PFT in MESMO 2 allowed it to have a
77 Fe-dependent, variable Si:N uptake ratio (Hutchins and Bruland, 1998; Takeda, 1998),
78 which is critical to simulate important features of the global ocean Si distribution.

79

80 MESMO 1 and 2 were assessed and calibrated by multi-objective tuning and extensive
81 model-data comparisons of transient tracers (anthropogenic carbon, CFCs), deep ocean
82 $\Delta^{14}\text{C}$, and nutrients (Matsumoto et al., 2008, 2013). These versions have been employed
83 successfully in a number of studies of global distributions of carbon and carbon isotopes
84 under various conditions of the past, present, and future (Cheng et al., 2018; Lee et al.,
85 2011; Matsumoto et al., 2010, 2020; Matsumoto and McNeil, 2012; Matsumoto and
86 Yokoyama, 2013; Sun and Matsumoto, 2010; Tanioka and Matsumoto, 2017; Ushie and
87 Matsumoto, 2012). Also, MESMO 1 and 2 have participated in model intercomparison
88 projects (Archer et al., 2009; Cao et al., 2009; Eby et al., 2013; Joos et al., 2013; Weaver et
89 al., 2012; Zickfeld et al., 2013).

90

91 In this contribution, we describe the third and latest version of MEMSO with a number of
92 substantial biogeochemical model modifications and new features that bring MESMO up to
93 date with the evolving and accumulating knowledge of the ocean biogeochemical cycle
94 (Table 1). There is no change in the physical model between MESMO 3 and MESMO 2. The
95 most significant new feature of MESMO 3 over the previous versions is the power law
96 formulation of flexible phytoplankton C:N:P ratio. Other new features include additional
97 PFT diazotrophs that carry out N-fixation, water column denitrification, the dependence of
98 organic matter remineralization on the dissolved oxygen (O_2) and temperature, and $CaCO_3$
99 production based on the concept of the residual nitrate potential growth. Also, we describe
100 the semi-labile DOM for P, N, and Fe (DOP_{sl} , DON_{sl} , and $DOFe_{sl}$), and the refractory DOM for
101 C, P, and N (DOC_r , DOP_r , and DON_r), which can be activated as an optional feature in MESMO
102 3. Some of these features have been described separately in different publications
103 (Matsumoto et al., 2020; Matsumoto and Tanioka, 2020; Tanioka and Matsumoto, 2017,
104 2020a). This work consolidates the descriptions of all these features in a single publication.

105

106 **2. Model Description**

107 Here we present the full set of biogeochemical equations of MESMO 3 as well as key model
108 parameters (Table 2). We describe only the biogeochemical source and sink terms and omit
109 the physical (advective and diffusive) transport terms that are calculated by the ocean
110 circulation model. We discuss the production terms first, followed by remineralization
111 terms, followed by conservation equations that incorporate both terms.

112

113 **2.1 Phytoplankton Nutrient Uptake**

114 NPP occurs in the top two vertical levels of the ocean domain above the fixed compensation
115 depth (z_c) of 100 m. Key parameter values are given in Table 2a. Nutrient uptake by
116 phytoplankton type i (Γ_i) depends on the optimal nutrient uptake timescale (τ_i), nutrients,
117 temperature (T), irradiance (I), and mixed layer depth (z_{ml}):

118

$$\Gamma_i = \frac{1}{\tau_i} \cdot F_{N,i} \cdot F_T \cdot F_l \cdot \max \left\{ 1, \frac{Z_c}{Z_{ml}} \right\} \quad 1$$

119

120 Subscript i refers to PFT (i =1: eukaryotes, i =2: cyanobacteria, i = 3: diazotrophs). The
 121 nutrient dependence $F_{N,i}$ is given by Liebig's law of minimum combined with Michael-
 122 Menten uptake kinetics of limiting nutrients: PO_4 , NO_3 , CO_2 , (aq), total dissolved iron (sum
 123 of free iron and ligand-bound iron; $FeT=Fe'+FeL$), and silicic acid ($Si(OH)_4$):

124

$$F_{N,i} = \min \left(\frac{[PO_4]}{[PO_4] + K_{PO_4,i}} \cdot [PO_4], \frac{[NO_3]}{[NO_3] + K_{NO_3,i}} \cdot [NO_3] \cdot Q_{N,i}^{-1}, \frac{[CO_2(aq)]}{[CO_2(aq)] + K_{CO_2,i}} \cdot [CO_2(aq)] \cdot Q_{C,i}^{-1}, \frac{[FeT]}{[FeT] + K_{FeT,i}} \cdot [FeT] \cdot Q_{Fe,i}^{-1}, \frac{[Si(OH)_4]}{[Si(OH)_4] + K_{Si(OH)_4}} \cdot [Si(OH)_4] \cdot Q_{Si}^{-1} \right) \quad 2$$

125

126 where $K_{X,i}$ is the half-saturation concentration of nutrient X for PFT i. Only eukaryotes (i=1)
 127 are limited by $Si(OH)_4$. Diazotrophs (i = 3) are not limited by NO_3 . Nutrient uptake Γ is
 128 based on the master nutrient variable P, and all other nutrient uptake is related to Γ by the
 129 uptake stoichiometry $Q_{X,i}$, where X is N, Fe, Si, or C. For example, $Q_{C,i} = \frac{1}{[P:C]_i}$ for PFT i. Thus,
 130 $Q_{C,i}$ is numerically equivalent to C:P for PFT i, but we write the equations in terms of P:C for
 131 numerical stability and convenience. The $Q_{X,i}$ ratios represent the flexible phytoplankton
 132 uptake stoichiometry and describe more fully in the following section 2.2.

133

134 The temperature dependence F_T of Equation 1 is given by:

135

$$F_T = \frac{T(^{\circ}C) + 2}{T(^{\circ}C) + 10} \quad 3$$

136

137 which is analogous to the commonly used $Q_{10} = 2$ relationship. Light limitation F_l of
 138 Equation 1 is described by a hyperbolic function:

$$F_T = \frac{I}{I + 20}$$

4

139

140 where I is the seasonally variable solar short-wave irradiance in W m^{-2} . Light is attenuated
141 exponentially from the ocean surface with a 20 m depth scale.

142

143 Nutrient uptake in Equation 1 has a dependence on z_{ml} , which is diagnosed using the σ_t
144 density gradient criterion (Levitus, 1982). Following the Sverdrup (1953) model of the
145 spring bloom, Equation 1 allows for the shoaling of z_{ml} relative to z_c to enhance nutrient
146 uptake.

147

148 **2.2 Phytoplankton uptake stoichiometry**

149 As noted above, all nutrients and O_2 are related to the main model currency P by $Q_{X,i}$. We
150 describe three different, mutually exclusive formulations in this section. The standard
151 formulation is the power law model (Matsumoto et al., 2020; Tanioka and Matsumoto,
152 2017). The other two (Linear model and Optimality-based model of stoichiometry) are
153 alternative formulations that have been coded, and the user can activate them (one at a
154 time) in place of the power law formulation. However, the alternative formulations are not
155 calibrated. Key parameter values are given in Table 2b for the power law formulation.

156

157 **2.2.1 Power law model of stoichiometry**

158 The uptake P:C and N:C ratios are calculated using the power-law formulation as a function
159 of ambient concentrations of phosphate [PO_4], nitrate [NO_3], temperature (T), and
160 Irradiance (I):

161

7

$$[P:C]_i = [P:C]_{0,i} \cdot \left(\frac{[PO_4]_i}{[PO_4]_0}\right)^{s_{PO_4,i}^{P:C}} \cdot \left(\frac{[NO_3]_i}{[NO_3]_0}\right)^{s_{NO_3,i}^{P:C}} \cdot \left(\frac{T}{T_0}\right)^{s_{T,i}^{P:C}} \cdot \left(\frac{I}{I_0}\right)^{s_{I,i}^{P:C}} \quad 5$$

$$[N:C]_i = [N:C]_{0,i} \cdot \left(\frac{[PO_4]_i}{[PO_4]_0}\right)^{s_{PO_4,i}^{N:C}} \cdot \left(\frac{[NO_3]_i}{[NO_3]_0}\right)^{s_{NO_3,i}^{N:C}} \cdot \left(\frac{T}{T_0}\right)^{s_{T,i}^{N:C}} \cdot \left(\frac{I}{I_0}\right)^{s_{I,i}^{N:C}} \quad 6$$

162

163 Equations 5 and 6 are the power-law equations that calculate the change in P:C and N:C for
 164 fractional changes in environmental drivers relative to the reference P:C and N:C,
 165 respectively (Matsumoto et al., 2020; Tanioka and Matsumoto, 2017). The exponents are
 166 the sensitivity factors determined by a meta-analysis (Tanioka and Matsumoto, 2020a).

167 Subscript "0" indicates the reference values (Table 2b). [We have hard bounds for the](#)
 168 [calculated P:C and N:C ratios to be within 26.6<C:P<546.7 and 2<C:N<30 as observed](#)
 169 [\(Martiny et al., 2013\).](#)

170

171 The P:C and N:C ratios from Equations 5 and 6 can then be converted to $Q_{N,i}$ and $Q_{C,i}$ for use
 172 in Equation 2.

173

$$Q_{C,i} = \frac{1}{[P:C]_i} \quad 7$$

$$Q_{N,i} = \frac{1}{[P:N]_i} = \frac{[N:C]_i}{[P:C]_i} \quad 8$$

174

175 2.2.2 Linear model of stoichiometry by Galbraith & Martiny

176 A much simpler, alternative formulation for P:C and N:C is the model of Galbraith & Martiny
 177 (2015) where P:C is a linear function of $[PO_4]$ (in μM), and N:C is a Holling type 2 functional
 178 form with a frugality behavior only at very low $[NO_3]$ (in μM). The same P:C and N:C values
 179 are applied to all three PFTs.

180

$$[P:C] = \frac{6.9 \cdot [PO_4] + 6.0}{1000} \quad 9$$

$$[N:C] = 0.125 + \frac{0.03 \cdot [NO_3]}{0.32 + [NO_3]} \quad 10$$

181

182 **2.2.3 Optimality-based model of stoichiometry**

183 The optimality-based model of phytoplankton growth is based on the chain model, which
184 connects the cellular P, N, and C acquisition by a chain of limitations, where the P quota
185 limits N assimilation and the N quota drives carbon fixation (Pahlow et al., 2013; Pahlow
186 and Oschlies, 2009, 2013). Resource-allocation of cellular P, N, and C among different
187 cellular compartments are derived from balancing energy gain from gross carbon fixation
188 and energy loss due to nutrient acquisition and light-harvesting. The optimality-based
189 model by Pahlow et al. (2013) computes C:N and C:P as a function of nutrient availability
190 (PO_4 and NO_3), irradiance, and day length. Temperature dependence was added by
191 Arteaga et al. (2014) following the simple logarithmic temperature dependence on
192 maximum nutrient uptake rate following (Eppley, 1972).

193

194 Different versions of this optimality-based model have previously been successfully
195 implemented in global ocean biogeochemical models, such as the Pelagic Interactions
196 Scheme for Carbon and Ecosystem Studies (PISCES) (Kwiatkowski et al., 2018, 2019) and
197 the University of Victoria Earth System Model (UVIC) (Chien et al., 2020; Pahlow et al.,
198 2020). However, as we are not describing any results in this paper, we will only mention
199 here that there is an option to calculate C:N:P using this stoichiometry model in MESMO 3.
200 The full description of the optimality-based stoichiometry model and its parameter
201 calibration are presented specifically for the UVic model elsewhere (Chien et al., 2020;
202 Pahlow et al., 2020).

203

204 **2.2.4 Stoichiometry of iron and silica**

205 Iron uptake stoichiometry $Q_{Fe,i}$ is calculated as a function of FeT following the power-law
206 formulation of Ridgwell (2001). Key parameter values are given in Table 2c.

207

$$Q_{Fe,i} = [Fe:P]_i = [Fe:C]_i \cdot Q_{C,i} \quad 11$$

$$[Fe:C]_i = 1.0 / ([C:Fe]_{min,i} + [C:Fe]_{ref,i} \cdot [FeT]^{-s^{Fe:C}_i}) \quad 12$$

208

209 For all PFTs, the power law exponent $s^{Fe:C}$ in Equation 12 is -0.65. The allowable Fe:C ratio
 210 is bounded at the low end by the hard-bound minimum Fe:C of 1:220,000. The scaling
 211 constant or $[C:Fe]_{ref,i}$ is set differently for PFTs, with eukaryotes having a higher base
 212 $[C:Fe]_{ref,i}$ than cyanobacteria and diazotrophs (115,623:1 and 31,805:1, respectively). The
 213 high end of the allowable Fe:C ratio is bounded by $[C:Fe]_{min,i}$ (i.e., maximum Fe:C) of
 214 15,000:1 for eukaryotes and 20,000:1 for cyanobacteria/diazotrophs. These parameters
 215 directly follow Ridgwell (2001), who fitted power-law functions to the experimental data
 216 (Sunda and Huntsman, 1995).

217

218 Silica uptake stoichiometry by eukaryotes Q_{Si} is a power law of total dissolved iron $[FeT]$
 219 and increases with a decrease in $[FeT]$ (Brzezinski, 2002). The power law exponent $s^{Si:N}$ is
 220 set to 0.7. The Si:N ratio is limited to a maximum of 18 and a minimum of 1.

221

$$Q_{Si} = [Si:P] = [Si:N] \cdot Q_{N,1} \quad 13$$

$$[Si:N] = \min \left([Si:N]_{max}, \max \left([Si:N]_{min}, \left(\frac{[FeT]}{0.5 \text{ nmol kg}^{-1}} \right)^{-s^{Si:N}} \right) \right) \quad 14$$

222

223 O_2 liberated by phytoplankton during photosynthesis per PO_4 consumed ($Q_{-O_2,i}$) is
 224 calculated from the uptake C:P and N:P ratios (Tanioka and Matsumoto, 2020b):

225

$$Q_{-O_2,i} = 1.1Q_{C,i} + 2Q_{N,i} \quad 15$$

226

227 **2.3 Production of POM and DOM**

228 In the top 100 m of the model domain, where phytoplankton P uptake occurs (i.e., $\Gamma_i > 0$,
 229 see section 2.1), NPP is immediately routed to POM and DOM pools (Figure 1). The
 230 production fluxes of POM, DOM_{sl} , and DOM_r from NPP are given as J_{prod} . Here we write the
 231 equations in terms of P, which is the master nutrient variable:

$$J_{prod_{POM_i}} = (1 - fDOM) \cdot \Gamma_i \quad 16$$

$$J_{prod_{DOM_{sl}}} = \sum_i (1 - fDOM_r) \cdot fDOM \cdot \Gamma_i \quad 17$$

$$J_{prod_{DOM_r}} = \sum_i fDOM_r \cdot fDOM \cdot \Gamma_i \quad 18$$

233
 234 The term $fDOM$ denotes the fraction of NPP that is routed to DOM as opposed to POM.
 235 Likewise, $fDOM_r$ is the fraction of DOM that is routed to DOM_r as opposed to DOM_{sl} . The
 236 value of $fDOM_r$ is not well known but estimated to be ~1% (Hansell, 2013), which we
 237 tentatively adopt in MESMO 3. If DOM_r is not selected in the model run, $fDOM_r = 0$. In
 238 previous versions of MESMO, $fDOM$ was assigned a constant value of 0.67. In reality, a large
 239 variability is observed locally for this ratio, ranging from 0.01-0.2 in temperate waters to
 240 0.1-0.7 in the Southern Ocean (Dunne et al., 2005; Henson et al., 2011; Laws et al., 2000). In
 241 MESMO 3, $fDOM$ is calculated as a function of the ambient temperature following Laws et
 242 al. (Laws et al., 2000):

$$fDOM = 1.0 - \min(0.72, \max(0.04, 0.62 - 0.02 \cdot T(^{\circ}C))) \quad 19$$

244
 245 This formulation gives low export efficiency (i.e., high $fDOM$) in the warmer regions
 246 compared to the colder high latitude regions. Locally, we impose fixed $fDOM$ upper and
 247 lower bounds of 0.96 and 0.28, respectively, as estimated from a previous study (Dunne et
 248 al., 2005).

249

Deleted: produced and

Deleted: 66

Deleted: w

253 In MEMSO 3, a new DOM production pathway below the production layer is available as an
 254 option. In previous MESMO versions, sinking POM was respired in the water column with
 255 the loss of O₂ directly to the dissolved inorganic forms (i.e., POC-->DIC, POP-->PO₄, and
 256 POP-->NO₃). In the new "deep POC split" pathway, sinking POM is simply broken down into
 257 DOM without the loss of O₂ **as in the production layer** (Figure 1). If DOM_r is selected in the
 258 model, the broken-down POM is further routed to both DOM_{sl} and DOM_r according to
 259 fDOM_r. If not, all of the broken down POM is converted to DOM_{sl}. Thus, when the deep POC
 260 split is activated, the presence of DOM in the deep ocean can be accounted for by *in situ*
 261 production of DOM and DOM_r in addition to DOM transport from the surface. Thus, the
 262 deep POC split pathway offers an alternative means to control deep ocean DOM
 263 distribution.

264

265 **2.4 Production of CaCO₃ and opal by eukaryotes**

266 In MESMO 2, opal production was associated with the large PFT and CaCO₃ production was
 267 associated with the "small" PFT. We recognize that coccolithophorids and diatoms, which
 268 are the producers of these biogenic tests, are both eukaryotes. Therefore, in MEMSO 3, we
 269 associate both CaCO₃ and opal production with the POM production by the same eukaryote
 270 PFT ($J_{prod_{POM1}}$):

271

$$J_{prod_{CaCO_3}} = r^{CaCO_3:POC} \cdot J_{prod_{POM1}} \cdot Q_{C,1} \quad 20$$

$$J_{prod_{opal}} = J_{prod_{POM1}} \cdot Q_{Si} \quad 21$$

272

273 The concept of the residual nitrate potential growth (RNPG) (Balch et al., 2016) is useful in
 274 allowing competition between diatoms and non-siliceous phytoplankton within the same
 275 PFT (Matsumoto et al., 2020). Typically, in the real ocean, non-Si phytoplankton are able to
 276 grow faster and dominate the community if Si concentration is low and diatom growth is Si
 277 limited. Otherwise, diatoms are more competitive, as they have higher intrinsic growth
 278 rates. The RNPG index recasts the ambient concentrations of NO₃ and Si(OH)₄ into potential
 279 algal growth rates:

280

$$RNPG = \frac{[NO_3]}{[NO_3] + K_{NO_3,1}} - \frac{[Si(OH)_4]}{[Si(OH)_4] + K_{Si(OH)_4}} \quad 22$$

281

282 If RNPG is more positive, the index indicates that nitrate-dependent growth exceeds silica-
283 dependent growth. Thus, non-Si phytoplankton are more competitive, and this leads to
284 higher CaCO₃ production. On the other hand, a more negative RNPG implies that silica
285 limitation for diatoms is relieved, leading to enhanced diatom growth and reduced CaCO₃
286 production. The RNPG index is incorporated in the calculation of the rain ratio $r^{CaCO_3:POC}$
287 presented in Equation 20 as:

288

$$r^{CaCO_3:POC} = r_0^{CaCO_3:POC} \cdot (\Omega - 1)^\eta \cdot \min(1, \max(0.1, RNPG)) \cdot k_{T,CaCO_3} \quad 23$$

289

290 Equation 23 indicates the base rain ratio $r_0^{CaCO_3:POC}$ (set to 0.30) is also modified by the
291 carbonate ion saturation state Ω by η (set to 1.28) by as well as by temperature (see
292 Ridgwell et al. (2007) and references therein):

293

$$\Omega = \frac{[Ca^{2+}][CO_3^{2-}]}{K_{sp}} \quad 24$$

$$k_{T,CaCO_3} = \min\left(1.0, \frac{T(^{\circ}C) + 2}{T(^{\circ}C) + 8}\right) \quad 25$$

294

295 K_{sp} is the solubility product of CaCO₃. The temperature dependency of CaCO₃ formation
296 ($k_{T,CaCO_3}$) is similar to that of Moore et al. (2004) where warmer temperatures favor the
297 growth of carbonate-bearing phytoplankton.

298

299 **2.5 Remineralization of POM and DOM**

300 Once produced, both POM and DOM undergo remineralization throughout the water
301 column. Key remineralization parameter values are given in Table 2d. Previously, POM

Deleted: te

Deleted: te

304 remineralization had a temperature dependence and decayed exponentially with depth
305 (Yamanaka et al., 2004). In MESMO 3, we incorporate an additional dependency on
306 dissolved oxygen following Laufkötter et al. (2017):
307

$$R_{POM_i} = V_{POM} \cdot e^{k_R T} \frac{[O_2]}{[O_2] + K_{O_2}} \cdot [POM_i] \quad 26$$

308
309 V_{POM} is the base remineralization rate, parameter k_R expresses the temperature sensitivity
310 of remineralization, and K_{O_2} is half-saturation constant for oxygen-dependent
311 remineralization. When the sediment model is not coupled, any POM that reaches the
312 seafloor dissolves completely to its inorganic form and is returned to the overlying water.
313

314 In MESMO 3, all forms of semi-labile DOM remineralize at the same rate. It is represented
315 by τ_{sl} , the inverse of the time scale of DOM_{sl} decay, which has been estimated previously to
316 be ~ 1.5 years (Hansell, 2013):
317

$$R_{DOM_{sl}} = \tau_{sl} \cdot [DOM_{sl}] \quad 27$$

318
319 All forms of DOM_r also remineralize at the same rate in MESMO 3. In total, there are three
320 optional, additive sinks of DOM_r in the model: slow background decay, photodegradation,
321 and degradation via hydrothermal vents (Figure 1). Observations clearly indicate that the
322 ^{14}C age of deep ocean DOC_r is 10^3 years (e.g., Druffel et al., 1992), much older than $DI^{14}C$.
323 Also, the deep ocean DOC_r concentration decreases modestly along the path of the deep
324 water from the deep North Atlantic to the deep North Pacific (Hansell and Carlson, 1998).
325 Thus, it is understood that there is a slow DOM_r background decay in the deep ocean. We
326 represent this ubiquitous process with τ_{bg} , which is the inverse of the background decay
327 time scale, estimated to be $\sim 16,000$ years (Hansell, 2013).

328
329 Observations to date indicate that photodegradation is a major sink of DOM_r (e.g., Mopper
330 et al., 1991). This process is believed to convert DOM_r that is upwelled from the ocean

331 interior into the euphotic zone into more labile forms of DOM. We represent
332 photodegradation with τ_{photo} , the inverse of the decay time scale, estimated to be ~70 years
333 (Yamanaka and Tajika, 1997). This occurs only in the surface.

334
335 Finally, observations of DOM emanating from different types of hydrothermal vents
336 indicate that they have variable impacts on the deep sea DOM_r (Lang et al., 2006). However,
337 the off-axis vents circulate far more seawater through the fractured oceanic crust than the
338 high temperature and diffuse vents and thus believed to determine the overall impact of
339 the vents on the deep sea DOM_r as a net sink (Lang et al., 2006). Here we assume simply
340 that seawater that circulates through the vents loses all DOM_r (i.e., $1/\tau_{vent} < \Delta t$, where Δt is
341 the biogeochemical model time step of 0.05 year). This means that the more seawater
342 circulates through the vents, the more DOM_r is removed: the total removal rate depends on
343 the vent flux of seawater H_{flux} . We implement the vent degradation of DOM_r in MESMO 3 by
344 first identifying the wet grid boxes located immediately above known mid-ocean ridges. We
345 then distribute the annual global H_{flux} of 4.8×10^{16} kg yr⁻¹ (Lang et al., 2006) equally among
346 those ridge-associated grid boxes. The grid cells contain a mass of seawater much greater
347 than the mass that circulates through vents in Δt (10^{21} kg vs. 10^{13} kg). Therefore, the
348 seawater mass in the vent grid cells that does not circulate through the vents in Δt is
349 subject only to background degradation in MESMO 3.

350

351 The three DOM_r sinks are not mutually exclusive. They can thus be combined to yield the
352 total DOM_r remineralization rate:

353

$$R_{DOM_r} = (\tau_{bg} + \tau_{photo} + \tau_{vent} \cdot \frac{SW_{flux_local}}{SW_{grid}}) \cdot [DOM_r] \quad 28$$

354

355 where SW_{flux_local} is the mass of seawater that circulates through the vents in each grid box
356 in Δt , and SW_{grid} is the total mass of seawater in the same grid box.

357

358 The amount of O₂ respired as a result of these POM and DOM remineralization processes is
359 related to the organic carbon pools by the respiratory quotients of POC and DOC, r_{-O₂:POC}
360 and r_{-O₂:DOC}, respectively. These are molar ratios of O₂ consumed per unit organic carbon
361 respired. They are variable and calculated from the ambient POM and DOM concentration
362 (Tanioka and Matsumoto, 2020b):

$$r_{-O_2:POC} = 1.1 + \frac{2[PON]}{[POC]} \quad 29$$

$$r_{-O_2:DOC} = 1.1 + \frac{2[DON]}{[DOC]} \quad 30$$

364

365 **2.6 Remineralization of CaCO₃ and opal**

366 Remineralization of CaCO₃ and opal particles occurs as they sink through the water column
367 and remains the same as in MESMO 2. Key parameter values are given in Table 2d.

368 Remineralization of CaCO₃ is a function of temperature similar to that of particulate organic
369 matter remineralization but without oxygen dependency. The temperature dependence
370 term k_R modifies the base remineralization rate V_{CaCO₃}:

371

$$R_{CaCO_3} = V_{CaCO_3} \cdot e^{k_R \cdot T} \cdot [CaCO_3] \quad 31$$

372

373 Opal remineralization in the water column follows Ridgwell et al. (2002). The rate of opal
374 remineralization R_{opal} is given by the product of normalized dissolution rate (r_{opal}), base
375 opal dissolution rate (k_{opal}), and opal concentration [opal]:

376

$$R_{opal} = r_{opal} \cdot k_{opal} \cdot [opal] \quad 32$$

$$r_{opal} = 0.16 \cdot \left(1 + \frac{T(^{\circ}\text{C})}{15}\right) \cdot u_{opal} + 0.55 \cdot \left(\left(1 + \frac{T(^{\circ}\text{C})}{400}\right)^4 \cdot u_{opal}\right)^{9.25} \quad 33$$

$$u_{opal} = \frac{[Si(OH)_4]_{eq} - [Si(OH)_4]}{[Si(OH)_4]_{eq}} \quad 34$$

377

378 r_{opal} is a function of temperature (T) and the degree of under-saturation (u_{opal}), which in
 379 turn is calculated from the ambient $[Si(OH)_4]$ and $[Si(OH)_4]$ at equilibrium. The
 380 equilibrium concentration is a function of ambient temperature:

381

$$\log_{10}([Si(OH)_4]_{eq}) = 6.44 - \frac{968}{T(K)} \quad 35$$

382

383 Without the sediment module of MESMO activated, both $CaCO_3$ and opal particles that
 384 reach the seafloor are completely dissolved back to inorganic forms.

385

386 **2.7 Conservation of organic matter and biogenic tests**

387 The time rate of change of the biogenic organic matter and tests are given by the sum of the
 388 production terms (i.e., sources) and the remineralization terms (i.e., sinks). The circulation-
 389 related transport terms are omitted as noted above, but the vertical transport due to
 390 particle sinking is included here. The sinking speed w is the same for all particles. The sum
 391 of POM_i of all the PFTs give the total POM concentrations:

392

$$\frac{\partial [POP]_i}{\partial t} = Jprod_{POP_i} - \frac{\partial}{\partial Z}(w[POP]_i) - R_{POP,i} \quad 36$$

$$\frac{\partial [POC]_i}{\partial t} = Jprod_{POP_i} \cdot Q_{C,i} - \frac{\partial}{\partial Z}(w[POC]_i) - R_{POC,i} \quad 37$$

$$\frac{\partial [PON]_i}{\partial t} = Jprod_{POP_i} \cdot Q_{N,i} - \frac{\partial}{\partial Z}(w[PON]_i) - R_{PON,i} \quad 38$$

$$\frac{\partial [POFe]_i}{\partial t} = Jprod_{POP_i} \cdot Q_{Fe,i} - \frac{\partial}{\partial Z}(w[POFe]_i) - R_{POFe,i} \quad 39$$

$$[POM] = \sum_i [POM]_i \quad 40$$

393

394 The time rate of change of $CaCO_3$ and opal is expressed in much the same way as POM:

395

$$\frac{\partial [CaCO_3]}{\partial t} = Jprod_{CaCO_3} - \frac{\partial}{\partial Z}(w[CaCO_3]) - R_{CaCO_3} \quad 41$$

$$\frac{\partial [opal]}{\partial t} = Jprod_{opal} - \frac{\partial}{\partial Z}(w[opal]) - R_{opal} \quad 42$$

396

397 The DOM pools have the production and remineralization terms without the particle

398 sinking term:

399

$$\frac{\partial [DOP_{sl}]}{\partial t} = J_{prod_{DOP_{sl}}} - R_{DOP_{sl}} \quad 43$$

$$\frac{\partial [DON_{sl}]}{\partial t} = J_{prod_{DON_{sl}}} - R_{DON_{sl}} \quad 44$$

$$\frac{\partial [DOC_{sl}]}{\partial t} = J_{prod_{DOC_{sl}}} - R_{DOC_{sl}} \quad 45$$

$$\frac{\partial [DOFe_{sl}]}{\partial t} = J_{prod_{DOFe_{sl}}} - R_{DOFe_{sl}} \quad 46$$

$$\frac{\partial [DOP_r]}{\partial t} = J_{prod_{DOP_r}} - R_{DOP_r} \quad 47$$

$$\frac{\partial [DON_r]}{\partial t} = J_{prod_{DON_r}} - R_{DON_r} \quad 48$$

$$\frac{\partial [DOC_r]}{\partial t} = J_{prod_{DOC_r}} - R_{DOC_r} \quad 49$$

400

401 2.8 Conservation of inorganic nutrients

402 The time rate of change of the inorganic nutrients have organic carbon production as sink
403 terms and remineralization as source terms. The production terms (J_{prod}) are zero below

404 the upper ocean production layer. Nutrients have a unit of mol element kg^{-1} **in the model.**

405

Deleted: generally

Deleted: μ

Deleted: , except for iron, whose unit is $nmol Fe kg^{-1}$.

$$\frac{\partial [PO_4]}{\partial t} = - \sum_i \Gamma_i + \sum_i R_{POP,i} + R_{DOP_{sl}} + R_{DOP_r} \quad 50$$

$$\frac{\partial [NO_3]}{\partial t} = - \sum_i \Gamma_i \cdot Q_{N,i} + \sum_i R_{PON,i} + R_{DON_{sl}} + R_{DON_r} + Fix_N - Den_N \quad 51$$

$$\frac{\partial [DIC]}{\partial t} = - \left(\sum_i \Gamma_i Q_{C,i} + Jprod_{CaCO_3} \right) + \sum_i R_{POC,i} + R_{DOC_{sl}} + R_{DOC_r} + R_{CaCO_3} + F_{gas,CO_2} \quad 52$$

$$\frac{\partial [ALK]}{\partial t} = - \left(2 \cdot Jprod_{CaCO_3} - \sum_i \Gamma_i Q_{N,i} \right) - \sum_i R_{PON,i} - R_{DON_{sl}} - R_{DON_r} - Fix_N + Den_N + 2 \cdot R_{CaCO_3} \quad 53$$

$$\frac{\partial [FeT]}{\partial t} = - \sum_i \Gamma_i Q_{Fe,i} + \sum_i R_{POFe,i} + R_{DOFe_{sl}} + R_{POM_{Fe}} + Aeolian_{Fe} \quad 54$$

$$\frac{\partial [Si(OH)_4]}{\partial t} = -Jprod_{opal} + R_{opal} \quad 55$$

$$\frac{\partial [O_2]}{\partial t} = \sum_i \Gamma_i \cdot Q_{-O_2,i} - \left(r_{-O_2:DOC} \cdot (R_{DOC_{sl}} + R_{DOC_r}) + \sum_i r_{-O_2:POC,i} \cdot R_{POC,i} \right) + 1.25 Den_N + F_{gas,O_2} \quad 56$$

409

410 In Equation 51, Fix_N is the N-fixation carried out by diazotrophs, and Den_N is the water
 411 column denitrification. There is an air-sea gas exchange term F_{gas} in Equations 52 and 56 for
 412 gaseous CO_2 and O_2 , respectively. In Equation 53, alkalinity increases with decreasing
 413 nitrate concentrations and increasing $CaCO_3$ dissolution. Equation 54 contains $R_{POM_{Fe}}$,
 414 which is an iron source that represents remineralization of the Fe' scavenged by sinking
 415 particles. These terms are explained in the following sections.

416

417 **2.9 Prognostic nitrogen cycle**

418 Biological production by diazotrophs is stimulated when the ambient NO_3 is low. Nitrogen
 419 fixed by diazotrophs during their growth is added to the marine NO_3 pool. The prognostic
 420 nitrogen fixation model employed here is similar to that used in the HAMOCC
 421 biogeochemical module (Paulsen et al., 2017):

422

$$Fix_N = F_3 \cdot Q_{N,3} \cdot I_{NO_3}, \quad 57$$

$$I_{NO_3} = \left(1.0 - \frac{[NO_3]^2}{K_{N_2} + [NO_3]^2} \right), \quad 58$$

423

424 where Fix_N is the nitrogen fixation rate and I_{NO_3} is the nitrate dependency term in
 425 quadratic Michaelis-Menten kinetics form with the half-saturation constant K_{N_2} . See Table
 426 2e for the values related to the N cycle.

427

428 Water-column denitrification is formulated in an approach similar to that of the original
 429 GENIE model (Ridgwell et al., 2007), in which 2 moles of NO_3 are converted to 1 mole of N_2
 430 and liberating 2.5 moles of O_2 as a byproduct:

431



432

433 Denitrification takes place in grid boxes, in which O_2 concentration is below a threshold
 434 concentration ($\text{O}_{2,\text{def}}$) and is stimulated if the total global inventory of NO_3 relative to PO_4 is
 435 high. In other words, denitrification can effectively act as negative feedback to nitrogen
 436 fixation. The threshold O_2 concentration ($\text{O}_{2,\text{def}}$) takes the minimum of the hard-bound O_2
 437 threshold concentration ($\text{O}_{2,\text{crit}}$) and the NO_3 to PO_4 ratio, scaled by a parameter k_D . The
 438 parameters $\text{O}_{2,\text{crit}}$ and k_D are calibrated to give the global denitrification rate of roughly
 439 100 Tg N yr^{-1} , which balances the total nitrogen fixation rate in the model.

440

$$Den_N = 0.8 \text{ [yr}^{-1}\text{]} \cdot \max\left(\left([O_2]_{def} - [O_2]\right), 0\right) \quad 60$$

$$[O_2]_{def} = \min\left(O_{2,crit}, k_D \cdot \frac{[NO_3]_{inventory}}{[PO_4]_{inventory}}\right) \quad 61$$

441

442 2.10 Prognostic iron cycle

443 The iron cycle in MESMO 3 remains the same as in MESMO 2. Key parameter values are
 444 given in Table 2e. The two species of dissolved iron (Fe' and FeL) are partitioned according
 445 to the following equilibrium relationship:

446

$$K_{ligand} = \frac{[FeL]}{[Fe'] \cdot [L]} \quad 62$$

447

448 where [L] is the ligand concentration, and K_{ligand} is the conditional stability constant. The
 449 sum of ligand and FeL is set at a constant value of 1 nmol kg⁻¹ everywhere. Iron is
 450 introduced into the model domain by a constant fraction (3.5 weight %) of aeolian dust
 451 deposition at the surface (F_{in}) following the prescribed modern flux pattern (Mahowald et
 452 al., 2006) with constant solubility (β):

453

$$S_{Fe} = \beta \cdot F_{in} \quad 63$$

454

455 Particle-scavenged iron POM_{Fe} (note the difference from $POFe$) is produced below the
 456 productive layer when sinking POM scavenges Fe' to sinking POM:

457

$$J_{Fe} = -\tau_{sc} \cdot K_o \cdot [POC]^{0.58} \cdot [Fe'] \quad 64$$

458

459 where τ_{sc} and K_o are empirical parameters that determine the strength of scavenging.

460 Remineralization of Fe scavenged to POM (POM_{Fe}) is identical in form to that of POM

461 remineralization:

462

$$R_{POM_{Fe}} = V_{POM} \cdot e^{k_{RT} \frac{[O_2]}{[O_2] + K_{O_2}}} \cdot [POM_{Fe}] \quad 65$$

463

464 The conservation equation of the particle scavenged iron is thus expressed as :

465

$$\frac{\partial [POM_{Fe}]}{\partial t} = J_{Fe} - \frac{\partial}{\partial z} (w [POM_{Fe}]) - R_{POM_{Fe}} \quad 66$$

466

467 Any scavenged iron that escapes remineralization in the water column reaching the
 468 seafloor is removed from the model domain in order to keep the total Fe inventory at a
 469 steady state.

470

471 2.11 Air-sea gas Exchange

472 The air-sea gas exchange formulation remains the same as in MESMO 2 and follows
 473 Ridgwell et al. (2007). It is the function of gas transfer velocity, the ambient dissolved gas
 474 concentration, and saturation gas concentration. The flux of CO₂ and O₂ gases across the
 475 air-sea interface is given by:

476

$$F_{gas,CO_2} = k \cdot ([CO_2]_{sat} - [CO_2]) \cdot (1 - A) \quad 67$$

$$F_{gas,O_2} = k \cdot ([O_2]_{sat} - [O_2]) \cdot (1 - A) \quad 68$$

477

478 where k is the gas transfer velocity, [CO₂]_{sat} and [O₂]_{sat} are saturation concentrations, and
 479 A is the fractional ice-covered area that is calculated by the physical model. Gas transfer
 480 velocity k is a function of wind speed (u) following Wanninkhof (1992) where Sc is the
 481 Schmidt Number for a specific gas:

482

Deleted: · ρ

Deleted: · ρ

Deleted: ρ is the density of seawater,

$$k = 0.31 \cdot u^2 \cdot \left(\frac{Sc}{660}\right)^{-0.5}$$

69

486

487 **3 Results and Discussion**

488 All new results from MESMO 3 presented here are from the steady state. On a single
 489 compute core at the Minnesota Supercomputing Institute, it takes approximately 1 hour to
 490 complete 1,000 years of MESMO 3 simulation. The "standard" MESMO 3 has the power law
 491 model of flexible stoichiometry but no DOM_r. The results from the standard model
 492 (hereafter just MESMO 3) are presented in Section 3.1, and the results from the DOM_r-
 493 enabled model are presented in Section 3.2. In Table 3, we summarize and compare key
 494 biogeochemical diagnostics from MESMO 3 against those from MESMO 2 and available
 495 observational constraints. The global NPP, as well as global export production of POC and
 496 opal, are comparable or somewhat lower in MESMO 3 than MESMO 2.

497

498 We relied on experience to calibrate MESMO 3 with the primary goal of reasonably
 499 simulating the phytoplankton community composition and C:N:P ratio (e.g. abundant
 500 cyanobacteria and high ratio for all PFTs in oligotrophic gyres). We tried to improve or at
 501 least preserve the gains that we achieved in earlier versions of MESMO in terms of the
 502 global distributions of PO₄, NO₃, O₂, Si(OH)₄, and FeT (Supplemental Figures S1, S2, S3, S4,
 503 and S5). Overall, there is a stronger nutrient depletion in the new model. For example, the
 504 surface PO₄ and NO₃ in MESMO 3 are now sufficiently depleted in the subtropical gyres but
 505 too low in the eastern equatorial Pacific when compared to the World Ocean Atlas (Figure
 506 S1; see RMSE in Table 3). It is a challenge for MESMO and other coarse resolution models to
 507 simulate narrow dynamical features such as equatorial upwelling and reproduce
 508 biogeochemical features with sharp gradients. The spatial pattern of POC export that drives
 509 this surface nutrient pattern is similar in the two models (Figure S2). In the 1D global
 510 profile, there is a marked improvement in the subsurface distribution of O₂ in MESMO 3
 511 over MESMO 2. Whereas the depth of the oxygen minimum was ~300 m in MEMOS 2, it is
 512 ~1000 m in both MESMO 3 and the World Ocean Atlas (Figure S3). At 1000 m, the O₂
 513 minimum is located in the far North Pacific in MESMO 3, whereas in the World Ocean Atlas

Deleted: , DOC,**Deleted:** For example, the global opal export production is nearly the same at 128-130 Tmol Si y⁻¹, while the global POC export is 9.4 Pg C y⁻¹ in MESMO 3 and 11.9 Pg C y⁻¹ in MESMO 2.**Deleted:** One reason for the lower POC export in the new model is that the global mean, production-layer fDOM, which was 0.66 everywhere in MESMO 2, increased to 0.71 in MESMO 3.

Before discussing the new features of MESMO 3, we note that the new model does just as well if not better than MESMO 2

Deleted: Overall**Deleted:** concentrations of**Deleted:** of the two models are both**Deleted:** but more so in MESMO 3, which is more in line with**Deleted:** T

530 it occurs in both the Northeast Pacific and the Arabian Sea. In contrast, the world ocean at
531 1000 m is too well-oxygenated in MESMO 2. We believe that the improved match in the O₂
532 minimum depth would help simulate denitrification in the correct depth range, and there is
533 a modest improvement in the data-model O₂ mismatch in terms of RMSE in MESMO 3 over
534 MESMO 2 (Table 3). The deepening of the O₂ minimum was achieved largely by increasing
535 the particle sinking speed, which tends to strengthen the biological pump and deplete the
536 surface nutrients. This also helps MESMO 3 preserves MESMO 2's surface Si(OH)₄ depletion
537 in much of the world ocean except in the North Pacific and Southern Ocean (Figure S4).
538 This is a feature captured by Si* < 0 (Si* = [Si(OH)₄] - [NO₃]) in observations (Sarmiento et al.,
539 2004) and simulated previously by MESMO 2 and now MESMO 3. Finally, surface FeT is also
540 depleted more strongly in MESMO 3 over MESMO2, except the North Atlantic, where
541 aeolian deposition of dust from the Sahara maintains a steady Fe supply (Figure S5).

542
543 In MESMO 3, we made no effort to calibrate all the semi-labile pools of DOM: DOC_{sl}, DOP_{sl},
544 DON_{sl}, and DOFe_{sl}. We note only that the surface DOC_{sl} concentration of 58 μmol kg⁻¹ and
545 DOC export production of 1.4 Pg C yr⁻¹ in MESMO 3 are higher than in MESMO 2 (24 μmol
546 kg⁻¹ and 0.4 Pg C yr⁻¹, respectively). The higher surface concentration is due to the longer τ_{sl}
547 in MESMO 3 (Table 2d). The global average of the temperature dependent fDOM in MESMO
548 3 is 0.69, which is slightly higher than the spatially uniform value of 0.67 in MESMO 2.

550 **3.1 Novel features of MESMO 3**

551 An important new feature of MESMO 3 is the representation of the primary producers by
552 three PFTs (Figure 2). The eukaryotes are characterized by the highest maximum growth
553 rate and high half-saturation constants. Thus, the eukaryotes are more dominant than the
554 other PFTs in the more eutrophic waters of the equatorial and polar regions (Figure 2a).
555 The cyanobacteria have smaller half-saturation constants and thus are more dominant in
556 the oligotrophic subtropical gyres (Figure 2c). The diazotrophs do not have NO₃ limitation
557 but have the lowest maximum growth rate. Thus it is much lower in abundance than the
558 other two PFTs generally, and outcompeted in transient blooms and thus excluded in
559 higher latitudes (Figure 2e).

Deleted: improvement

Deleted: comes

Deleted: in part

Deleted: from

Deleted: adjusting

Deleted:

Deleted: and fDOM

Deleted: As for Si(OH)₄,

568

569 Figure 2 also indicates that all three PFTs show Fe limitation in the Southern Ocean.

Deleted: 1

570 Outside the Southern Ocean, the eukaryotes are primarily limited by $\text{Si}(\text{OH})_4$ (Figure 2b).

Deleted: 1b

571 ~~As far as organic carbon is concerned, we consider the eukaryotes to basically represent~~
572 ~~diatoms, which are arguably the most important agent of organic carbon export. In this~~
573 ~~context, the widespread silica limitation for eukaryotes would be consistent with the~~
574 ~~notions that silica uptake by diatoms should be limited in ~60% of the world surface ocean~~
575 ~~(Ragueneau et al. 2000) and that much the world ocean thermocline is filled with silica-~~
576 ~~depleted water ($\text{Si}^* < 0$ as noted above). On the other hand, the cyanobacteria are largely~~

Deleted: , while

577 limited by NO_3^- outside the Southern Ocean (Figure 2d). The diazotrophs are limited by iron
578 in much of the world ocean except in the Atlantic basin (Figure 2f), where surface PO_4 is
579 strongly depleted in both observations (Mather et al., 2008) and in our model (Figure S1).

Deleted: is

580

581 Figure 3 illustrates the influence of the RNPG index, which was implemented in MESMO 3
582 to allow for the effect of competition between diatoms and coccolithophores within the
583 same PFT (Equations 22 and 23). The eukaryote NPP (Figure 3a) is effectively split into two
584 parts: one is associated with diatoms and opal production (Figure 3b), and the other is
585 associated with coccolithophores and CaCO_3 production (Figure 3c). According to the RNPG
586 index, opal production is simulated more in the higher latitudes of the Southern Ocean and
587 the North Pacific, where surface $[\text{Si}(\text{OH})_4]$ is abundant. Elsewhere, CaCO_3 production is
588 relatively larger. The decoupling is prominent in the North Indian. Note that the spatial
589 pattern of CaCO_3 production is quite different in MEMOS 3 (Figure 3c) and MESMO 2
590 (Figure 3d), because CaCO_3 production was associated in MESMO 2 with the "small" PFT,
591 which corresponds to the cyanobacteria PFT in MESMO 3.

592

593 The global pattern of the mean C:P uptake ratio in the production layer is shown in Figure
594 4. Consistent with observations (Martiny et al., 2013), the simulated C:P ratio of the
595 phytoplankton community is elevated in the oligotrophic subtropical gyres and low in the
596 eutrophic polar waters (Figure 4a). The community C:P ratio exceeds 200 in the gyres and
597 reaches as low as 40-50 in the Southern Ocean. The community C:P has contributions from
598 both physiological effects (i.e., environmental drivers acting on each PFT's C:P ratio) and

Deleted: s

604 taxonomic effects (i.e., the shift in the community composition changes the weighting of
605 each PFT's C:P ratio). Figure 4b shows that the community C:P is high in oligotrophic gyres
606 because cyanobacteria and to a lesser extent diazotrophs dominate the community, and
607 their C:P ratio is high. Conversely, the community C:P is low in the polar waters because the
608 eukaryotes dominate and their C:P ratio is low. For both eukaryotes and cyanobacteria,
609 their C:P is high in oligotrophic subtropical gyres because PO_4 is low (Figure 4c and d). This
610 physiological effect is larger in eukaryotes than cyanobacteria because the former has
611 greater sensitivity (i.e., larger sensitivity factor $s_{PO_4}^{P:C}$, Equation 5, Table 2b). However, the
612 cyanobacteria PFT's C:P ratio has an additional sensitivity to temperature (i.e., $s_T^{P:C} \neq 0$)
613 that elevates their C:P in the lower latitudes. We do not show the C:P ratio for diazotrophs
614 because it is very similar to that of cyanobacteria (Figure 4b, d).

615

616 In order to gain more insights into the spatial patterns of the C:P ratio (Figure 4), we
617 examined the relationships between the C:P and C:N ratios and the four possible
618 environmental drivers for eukaryotes and cyanobacteria (Figure 5; again, diazotrophs are
619 not shown). The red plots show that there is a causal relationship between the ratios and
620 the drivers as formulated by the power law model (Equations 5 and 6). The black plots
621 show the absence of a causal relationship. For example, the C:P ratio of both eukaryotes
622 and cyanobacteria are strongly correlated with PO_4 because there is a causal relationship
623 (Figure 5a, b shown in red). Similarly, the C:N ratio of the same two PFTs have a strong
624 correlation with PO_4 (Figure 5c, d in black), but there is actually not a causal relationship
625 (i.e., $s_{PO_4}^{N:C} = 0$, Table 2b). The C:N- PO_4 correlation exists, simply because the nutrients are
626 well correlated. Similarly, because temperature and photosynthetically active radiation
627 (PAR) tend to be correlated via latitude, the stoichiometry has a similar correlation to the
628 two drivers. For example, cyanobacteria C:P has a strong correlation with both
629 temperature and PAR (Figure 5j, 4n), but only the temperature is a real driver. Figure 5
630 indicates which are the dominant drivers of the C:N:P ratio in MESMO 3. For the eukaryote
631 C:P ratio, it is PO_4 . For the cyanobacteria C:P ratio, the important drivers are temperature
632 and PO_4 . For the C:N ratio for both eukaryotes and cyanobacteria, NO_3 is more important
633 than PAR. Figure 5 also serves to remind us that correlation does not indicate causation.

Deleted: partly

Deleted: in part

Deleted: of one of the most basic lessons of statistics,

637

638 Figure 6 shows the community C:P and C:N ratios plotted against the four environmental
639 drivers. Unlike Figure 5, which reflected the individual PFT's physiological response, Figure
640 6 includes the effect of taxonomy as well. Still, the effects of PO_4 and temperature are
641 clearly visible on the community C:P ratio. Both low $[\text{PO}_4]$ and warmer waters are found in
642 the lower latitudes, so the P frugality and temperature effects are additive. The effect of
643 NO_3 on the community C:N ratio is also very clear, but the effect of PAR is not as clear. Thus
644 overall, the physiological effects seen in the PFT-specific C:N:P are obvious in the
645 community C:N:P ratio.

646

647 **3.2 DOM_r-enabled MESMO 3**

648 In MESMO 2, DOC_{sl} was a standard state variable. In MESMO 3, other forms of DOM are
649 available as options. They are the semi-labile forms of DOM: DOP_{sl} , DON_{sl} , and DOFe_{sl} ; and
650 the refractory forms of DOM: DOC_{r} , DOP_{r} , and DON_{r} . MESMO 3 is not yet calibrated with
651 respect to all the DOM variables, but here we demonstrate their potential use in future
652 biogeochemical investigations by presenting steady state DOM results from the model
653 experiment *LV* (experiment ID: [210310m](#)). In this run, all three sinks of DOM_{r} are activated:
654 slow background decay, photodegradation, and degradation in hydrothermal vents.

655

656 The experiment name *LV* stands for "literature values." In *LV*, we use the literature values
657 for the key DOM remineralization model parameters (Table 2d) and $f\text{DOM}_{\text{r}} = 0.01$ (Hansell,
658 2013). All other model parameter values in the *LV* run are identical to the standard MESMO
659 3 model (Table 2). The black lines in Figure 7 show the global mean vertical profiles of the
660 total DOC ($\text{DOC}_{\text{t}} = \text{DOC}_{\text{sl}} + \text{DOC}_{\text{r}}$) in solid line and DOC_{r} in dashed line. Qualitatively, the
661 simulated profiles are consistent with the observations, showing a near-uniform DOC_{r}
662 concentration and a DOC_{sl} profile that rapidly with depth in the top few hundred meters
663 (Hansell, 2013). However, the simulated values reach $130 \mu\text{mol kg}^{-1}$ in the surface, which is
664 approximately twice the observations. More typically, the observed DOC_{r} is $30\sim 40 \mu\text{mol kg}^{-1}$
665 ¹, and the observed DOC_{sl} attenuates with depth from $30\sim 40 \mu\text{mol kg}^{-1}$ near the surface. So

666 their sum, which is represented by DOC_t , is approximately $60\text{-}80 \mu\text{mol kg}^{-1}$ at the surface in
667 observations.

668

669 Figure 8 adds a lateral perspective to Figure 7. The rapid DOC_t attenuation in the vertical is
670 strong in the lower latitudes where stratification is generally stronger. The transport of
671 DOC_{sl} from the surface to deeper waters is evident in the high latitudes of the North
672 Atlantic and the Southern Ocean. The DOC_t change in the deep ocean is limited.

673 Observations of deep ocean DOC_t indicates a reduction by 29% or $14 \mu\text{mol kg}^{-1}$ from the
674 deep North Atlantic to the deep North Pacific (Hansell and Carlson, 1998). Figure 8 shows
675 that the deep ocean DOC_t gradient in LV is approximately $10 \mu\text{mol kg}^{-1}$ from $70\text{-}75 \mu\text{mol kg}^{-1}$
676 1 in the North Atlantic to $<65 \mu\text{mol kg}^{-1}$ in the North Pacific.

677

678 The horizontal DOC_t distributions from the LV run can also be compared to a global
679 extrapolation based on an artificial neural network (ANN) of the available DOC_t data
680 (Roshan and DeVries, 2017). At the surface, the extrapolation indicates higher DOC_t
681 concentrations in the subtropical gyres (Figure 9a), while our simulation does not clearly
682 delineate the gyres (Figure 9c). In our model, $f\text{DOM}$ is temperature-dependent and strongly
683 controls the production of DOM. The surface DOC_t is thus more elevated in the lower
684 latitudes. Interestingly, the ANN study diagnosed higher rates of DOM production in the
685 subtropical gyres. Since the oligotrophic subtropical gyres have low NPP, the diagnosis
686 would thus suggest that somehow $f\text{DOM}$ is higher in the gyres. At depths, both the
687 extrapolated and simulated DOC_t show a gradual decline in concentrations from the North
688 Atlantic to the North Pacific (Figure 9b, d). The highest deep DOC_t in the LV run is seen just
689 south of Greenland, where convection occurs in the model.

690

691 Finally, we show that the deep ocean radiocarbon aging is larger in DIC than in DOC_t in the
692 model (Figure 10). The North Pacific-North Atlantic $\Delta^{14}\text{C}$ gradient is roughly -100‰ for
693 DIC and -70‰ for DOC_t . The oldest DOC_t $\Delta^{14}\text{C}$ is approximately -430‰ in the North Pacific.
694 If ^{14}C decay were the only mechanism of change along the path of the deepwater
695 circulation, the $\Delta^{14}\text{C}$ gradient should be quite similar between DIC and DOC_t , which are both

696 dissolved phases and transported passively by the same circulation. The one potentially
697 important difference is that the addition of the relatively young DI^{14}C and DO^{14}C to the
698 deep ocean by the "deep POC split" (see Section 2.3) impacts $\text{DOC}_t \Delta^{14}\text{C}$ more than $\text{DIC} \Delta^{14}\text{C}$,
699 because DOC_t is two orders of magnitude lower in concentration than DIC.

700

701 In observations, the aging of DIC and DOC_t is reportedly similar in the Antarctic Bottom
702 Water (below 4000 m) of the deep Pacific (Druffel et al., 2019). This may be explained by
703 the fact that there would not be much deep POC split occurring so deep in the ocean. The
704 North Pacific-North Atlantic $\Delta^{14}\text{C}$ gradient, accounting for thermonuclear bomb ^{14}C , may be
705 as large as -100‰ for DOC_t (about -550‰ in the deep Pacific and -456‰ in the deep
706 Atlantic) (Druffel et al., 2019). This gradient is not rigorously determined, because there is
707 not enough data to do an objective analysis. Therefore, the equivalent $\Delta^{14}\text{C}$ gradient for DIC
708 cannot be determined. However, the DIC $\Delta^{14}\text{C}$ endmember values by inspection (about -
709 250‰ in the deep Pacific and -70‰ in the deep Atlantic) (Matsumoto and Key, 2004)
710 indicate a clearly larger $\Delta^{14}\text{C}$ gradient for DIC than DOC_t as simulated by the experiment *LV*.

711

712 One lesson from the data-*LV* run mismatch in the overall DOC_t concentration (Figure 7) and
713 surface DOC_t pattern (Figure 9) is that the parameter values from the literature do not fully
714 capture the DOC cycle and/or MESMO 3 is still lacking some important DOC process. In *LV*,
715 the surface DOC_t is too high because DOC_r is too high, while DOC_{sj} is not unreasonable
716 (Figure 7). DOC_r is too high because there is too much DOC_r production (e.g., $\text{fDOM}_r=1\%$ is
717 too large), there is too little DOC_r degradation (e.g., one of the DOM decay mechanisms is
718 too slow; Equation 28 and Table 2d), or some combination of both. For example, fDOM_r is a
719 key parameter that is not well constrained by observations. Had we used 0.2% instead of
720 1% for fDOM_r , the global mean surface DOC_t drops to $76 \mu\text{mol kg}^{-1}$ (red line, Figure 7),
721 consistent with observations. For achieving a better surface DOC_t pattern, we may need a
722 different formulation of fDOM that is, for example, negatively related to nutrient
723 concentrations so that fDOM increases in the oligotrophic subtropical gyres (Roshan and
724 DeVries, 2017).

725

726 Another lesson from the DOM modeling exercise is that it is important to simulate DOP_r
727 reasonably well in order to preserve the favorable results we achieved in MESMO 3 with
728 respect to biological production and the phytoplankton C:N:P ratio. We find that in the
729 experiment *LV*, the global mean DOP_r concentration becomes steady at $0.45 \mu\text{mol-P kg}^{-1}$. In
730 observations, the mean DOC_r is about $40 \mu\text{mol-C kg}^{-1}$, and the $DOC_r:DOP_r$ ratio is estimated
731 to be $\sim 1370:1$ (Letscher and Moore, 2015), so DOP_r concentration should only be roughly
732 $0.03 \mu\text{mol-P kg}^{-1}$. Thus, the simulated $DOP_r=0.45 \mu\text{mol-P kg}^{-1}$ is an order of magnitude too
733 high. Because there is more P in the form of DOP_r in *LV*, the oceanic inventory of PO_4
734 declines, causing a nearly 10% drop in export production compared to the standard
735 MESMO 3. In *LV*, the decline in the surface ocean PO_4 that accompanies the change in the
736 PO_4 inventory acts on the phytoplankton physiology (i.e., P effect on C:P in Equation 5),
737 which leads to a large rise in the global mean phytoplankton community C:P export ratio
738 from 113:1 to 127:1. The implementation of preferential remineralization of DOP_r (and
739 DON) over DOC_r (Letscher and Moore, 2015) is one way to deal with the problem of too high
740 DOP_r concentrations.

741

742 3.3 Large-scale patterns of N_2 fixation and denitrification

743 The modeled habitat of diazotrophs is concentrated in tropical and subtropical waters
744 between 40°S and 40°N and limited by iron (Figure 1e, f). Most noticeably in North Pacific
745 subtropical gyre, diazotrophs constitute $\sim 40\%$ of total NPP. The latitudinal extent of
746 diazotrophs is mainly determined by surface nitrate availability and physical factors such
747 as surface temperature and irradiance. Low nitrate availability in subtropical gyres gives
748 diazotrophs a competitive advantage over small cyanobacteria. Warm temperature and
749 high irradiance also critical physical factors that drive the growth of diazotrophs in the
750 model.

751

752 The modeled global depth-integrated N_2 fixation is 101 Tg N yr^{-1} (Table 3), and this value
753 falls well within the range of observational and geochemical constraints of 80 – 200 Tg N
754 yr^{-1} (Landolfi et al., 2018). In MESMO 3, N_2 fixation occurs in the North Pacific and mid-to-
755 low latitudes of the Atlantic basin (Supplementary Figure S6). where diazotrophs are

Deleted: Given that

Deleted: be on the order of

Deleted: 109

Deleted: In general,

Deleted: regions where the diazotroph's productivity is high, such as ...

762 **generally more abundant (Figure 2e)**. The elevated N₂ fixation rate in the North Pacific,
763 where nitrate limits eukaryotes and cyanobacteria (Figure 2b, d), can be explained by the
764 healthy growth of diazotrophs, which is not limited by N. In the subtropical and tropical
765 Atlantic and the Indian Ocean, high N₂ fixation is driven by elevated C:P and N:P ratio
766 (Figure 4), exemplified by low phosphate availability and warm surface temperature. This
767 spatial pattern agrees with a recent inverse model study (Wang et al., 2019), which showed
768 an elevated N₂ fixation rate in subtropical gyres.

Deleted: 1b

769
770 Global water-column denitrification is **101 Tg N yr⁻¹** (Table 3) and is equal to the global N₂
771 fixation because the model has reached steady state. Denitrification is restricted to the
772 subpolar North Pacific (Figure S6), where sub-surface oxygen concentration is significantly
773 depleted (Figure S3d). Enhanced denitrification in this region is in qualitative agreement
774 with a previous modeling study (Bianchi et al., 2018), which showed the anaerobic niche
775 due to particle microenvironments can significantly expand the hypoxic expanses in the
776 North Pacific. However, the extent of denitrification in our model **does not include the**
777 **eastern equatorial Pacific and northern Indian, which are important** hotspots for
778 denitrification (Codispoti, 2007; Deutsch et al., 2007). This issue is typical of coarse-
779 resolution global ocean biogeochemistry models that lack spatial resolution in reproducing
780 intense upwelling (Marchal et al., 1998; Najjar et al., 1992; Yamanaka and Tajika, 1997).

Deleted: 109

Deleted: s

Deleted: Eastern

Deleted: N

Deleted: Ocean

Deleted: typically considered as the main

781
782 Finally, the ratio of the global inventories of NO₃ and PO₄ **in MESMO 3 is just about 16** at
783 steady state, **consistent with observations** (Gruber and Sarmiento, 1997). One key model
784 parameter in **this regard is** the nitrate uptake half saturation constant of diazotrophs, K_{NO_{3,3}}
785 in Equation 2. A large value of K_{NO_{3,3}} will make it hard for diazotrophs to obtain fixed N
786 from NO₃, which would facilitate N₂ fixation and pushes up the global N/P ratio. With a
787 smaller value of K_{NO_{3,3}}, diazotrophs will more easily uptake NO₃, thus depressing N₂
788 fixation, lowering the global N/P ratio.

Deleted: we note that an important feature of the global ocean that is faithfully simulated in MESMO 3 is that

Deleted: <

Deleted: achieving this result was

789

790 4. Conclusions

791 MESMO 3, the third and latest version of MESMO, is comprehensively described here. With
792 a fully flexible C:N:P ratio in three PFTs, a prognostic N cycle, and more mechanistic

804 schemes of organic matter production and remineralization, MESMO 3 reflects the evolving
805 and accumulating knowledge of the ocean biogeochemistry. The model thus remains an
806 effective tool for investigations of the global biogeochemical cycles especially on long time
807 scale given the model's computational efficiency. In particular, MESMO 3 holds promise for
808 studying the marine DOM cycle. The optional features of MESMO 3 include the semi-labile
809 and refractory pools of C, P, N, and Fe. The fact that the literature values regarding the
810 present marine DOM cycle are unable to simulate key observations indicates an
811 opportunity for MESMO 3 to contribute to an improved understanding of the marine DOM
812 cycle.

813

814 **Code availability**

815 The complete code of MESMO version 3.0 and results presented here are available at
816 GitHub <https://github.com/gaia3intc/mesmo.git> and have a DOI:
817 10.5281/zenodo.4403605.

818

819 **Author contribution**

820 KM, TT, and JZ developed the model code. KM performed the simulations, carried out
821 analyses, and archived the model code and results. KM and TT wrote the paper.

822

823 **Acknowledgements**

824 This work was funded by the US National Science Foundation (OCE-1827948). Numerical
825 modeling and analysis were carried out using resources at the University of Minnesota
826 Supercomputing Institute.

827

828 **Tables**

829

830 **Table 1.** MESMO Development

831 PFT = phytoplankton functional types. MESMO2 PFTs are LG = large/diatoms and SM = small.
832 MESMO 3 PFTs are Eu = eukaryotes, Cy = cyanobacteria, and Dz = diazotrophs. OM = organic
833 matter. RNPG = residual nitrate potential growth. T = temperature. PAR = photosynthetically
834 active radiation. fDOM = fraction of NPP routed to dissolved organic matter (DOM). The two
835 types of DOM are semi-labile (DOC, DOP, DON, and DOFe) and refractory (DOCr, DOPr, and
836 DONr). Carbon isotopes (¹²C, ¹³C, and ¹⁴C) are calculated separately for DOC and DOCr. The
837 run ID is 210310m for the MESMO 3 experiment LVR and 210310o for the experiment LVR
838 with fDOM_r=0.2%.

839
840

841 **Table 2.** MESMO 3 Biogeochemical Model Parameters Values

842

843 **Table 3.** Key Biogeochemical Model Diagnostics

844 ^aNPP for MESMO 2 was unavailable as a model output and therefore estimated from POC
845 and fDOM=0.67. ^bNPP (in terms of C) is needed in the calculation of the PFT abundance. The
846 root mean square error (RMSE) of the simulated P, N, Si, and O₂ distributions from MESMO
847 2 and 3 was calculated relative to the World Ocean Atlas 2018 gridded data (Garcia et al.
848 2018, 2019). The model-data comparison is made in the top 100 m for nutrients and below
849 100 m for O₂. WOA18 was regridded to the MESMO 3 grid to calculate the RMSE.

850
851

852 References for independent constraints: (1) global NPP (Carr et al., 2006); (2) global POC
853 export (DeVries and Weber, 2017); (3) global DOC export assumed to be 20% of total
854 carbon export (Hansell et al., 2009; Roshan and DeVries, 2017); (4) global opal (Dunne et
855 al., 2007); (5) global CaCO₃ export (Berelson et al., 2007); (6) global N fixation and
856 denitrification rates (Landolfi et al., 2018); (7) uptake C:N:P ratio is based on POM
857 measurements (Martiny et al., 2013); (8) export C:N:P ratio is assumed to equal the
858 subsurface remineralization ratio (Anderson and Sarmiento, 1994); (9) Deep O₂ from
859 WOA18 below 100 m (Garcia et al., 2019).

860

861

862

863

Deleted: ^aNPP for MESMO 2 was unavailable as a model output and therefore estimated from POC and fDOM=0.66. ^bThe calculation of the PFT abundance requires NPP in terms of P. NPP was unavailable as a model output for MESMO 2, so PFT % was estimated from POC export.

Deleted: 13

Deleted: (Garcia et al., 2013).

871 **Figures**

872

873 **Figure 1.** Schematic diagram of DOM cycling in MESMO 2 versus MESMO 3. In the new
874 model, DOM_r can be activated. DOM_r is produced from POM breakdown, which can occur in
875 the production layer or throughout the water column in the "deep POC split." Possible
876 DOM_r remineralization mechanisms are the slow background degradation that occurs
877 everywhere, thermal degradation in hydrothermal vents, and photodegradation in the
878 surface. See text for details.

879

880 **Figure 2.** NPP-based surface phytoplankton functional type (PFT) abundance and nutrient
881 limitation in MESMO 3. Fractional abundance and nutrient limitation for eukaryotes (a, b),
882 cyanobacteria (c, d), and diazotrophs (e, f).

883

884 **Figure 3.** Eukaryote production in MESMO 3 and $CaCO_3$ export in MESMO 2. In MESMO 3,
885 eukaryote NPP (a) is linked to both opal export (b) and $CaCO_3$ export (c) but the two export
886 productions are differentiated by the residual nitrate potential growth (RNPG). Compare
887 $CaCO_3$ export in MESMO 3 (c) to MESMO 2 (d). Unit = $mol\ m^{-2}\ year^{-1}$.

888

889 **Figure 4.** Uptake C:P ratio in the top 100 m in MESMO 3: (a) phytoplankton community C:P,
890 (b) zonal mean C:P of all three PFTs and phytoplankton community, (c) eukaryote C:P, and
891 (d) cyanobacteria C:P. The colors in (b) indicate: black = community C:P, red = eukaryote
892 C:P, green = cyanobacteria C:P, and blue = diazotroph C:P. Also, (b) shows the range of
893 observed C:P ratio binned by latitude (Martiny et al., 2013).

894

895 **Figure 5.** Scatter plots of surface ocean eukaryote and cyanobacteria C:P and C:N vs.
896 environmental drivers in MESMO 3. Columns: 1 = eukaryote C:P, 2 = cyanobacteria C:P, 3 =
897 eukaryote C:N, and 4 = cyanobacteria C:N. Rows: 1 = PO_4 , 2 = NO_3 , 3 = temperature, and 4 =
898 PAR. Red indicates causal relationship according to the power law formulation of flexible
899 C:N:P ratio. PAR = photosynthetically active radiation in $W\ m^{-2}$.

900

Deleted: The effect of the residual nitrate potential growth (RNPG) on the eukaryote production in MESMO 3. Eukaryote NPP (a), opal export (b), and $CaCO_3$ export (c) in MESMO 3. $CaCO_3$ export in MESMO 2 (d). Unit = $mol\ m^{-2}\ year^{-1}$.

905 **Figure 6.** Scatter plots of surface ocean community C:P and C:N vs environmental drivers in
906 MESMO 3.

907

908 **Figure 7.** Global mean vertical profiles of DOC from the DOM_R-enabled MESMO 3. DOC_t
909 ($\text{DOC}_{\text{gl}} + \text{DOC}_{\text{pr}}$, black line) and DOC_r (black dashed line) from the *LV* run. Red line is DOC_t
910 after reducing fDOM_r from 1% in *LV* to 0.2% ([Experiment 210310o](#)). Unit = $\mu\text{mol kg}^{-1}$.

911

912 **Figure 8.** Global depth-latitude transect of DOC_t from the DOM_R-enabled MESMO 3 *LV* run.
913 Transects are N-S along 25°W in the Atlantic, E-W along 60°S in the Southern Ocean, and N-
914 S along 165°E in the Pacific. Unit = $\mu\text{mol kg}^{-1}$.

915

916 **Figure 9.** Assessment of surface and deep ocean DOC_t from the DOM_R-enabled MESMO 3 *LV*
917 run. Data-derived DOC_t distributions in the top 100 m (a) and 2500-4000 m (b). Model-
918 simulated DOC_t distributions in the top 100 m (c) and 2500-4000 m (d). Date-derived DOC_t
919 are from Roshan and DeVries (Roshan and DeVries, 2017). Unit = $\mu\text{mol kg}^{-1}$.

920

921 **Figure 10.** $\Delta^{14}\text{C}$ of deep ocean DIC (a) and DOC_t (b) from the DOM_R-enabled MESMO 3 *LV*
922 run. Vertical average over 2500-4000 m water depth. Unit = ‰.

923

924 **References:**

- 925 Anderson, L. A. and Sarmiento, J. L.: Redfield ratios of remineralization determined by
926 nutrient data analysis, *Global Biogeochem. Cycles*, 8(1), 65–80,
927 doi:10.1029/93GB03318, 1994.
- 928 Archer, D., Eby, M., Brovkin, V., Ridgwell, A., Cao, L., Mikolajewicz, U., Caldeira, K.,
929 Matsumoto, K., Munhoven, G., Montenegro, A. and Tokos, K.: Atmospheric Lifetime of
930 Fossil Fuel Carbon Dioxide, *Annu. Rev. Earth Planet. Sci.*, 37(1), 117–134,
931 doi:10.1146/annurev.earth.031208.100206, 2009.
- 932 Arteaga, L., Pahlow, M. and Oschlies, A.: Global patterns of phytoplankton nutrient and light
933 colimitation inferred from an optimality-based model, *Global Biogeochem. Cycles*,
934 28(7), 648–661, doi:10.1002/2013GB004668, 2014.
- 935 Balch, W. M., Bates, N. R., Lam, P. J., Twining, B. S., Rosengard, S. Z., Bowler, B. C., Drapeau, D.
936 T., Garley, R., Lubelczyk, L. C., Mitchell, C. and Rauschenberg, S.: Factors regulating the
937 Great Calcite Belt in the Southern Ocean and its biogeochemical significance, *Global*
938 *Biogeochem. Cycles*, 30(8), 1124–1144, doi:10.1002/2016GB005414, 2016.
- 939 Berelson, W. M., Balch, W. M., Najjar, R., Feely, R. A., Sabine, C. and Lee, K.: Relating
940 estimates of CaCO₃ production, export, and dissolution in the water column to
941 measurements of CaCO₃ rain into sediment traps and dissolution on the sea floor: A
942 revised global carbonate budget, *Global Biogeochem. Cycles*, 21(1), 1–15,
943 doi:10.1029/2006GB002803, 2007.
- 944 Bianchi, D., Weber, T. S., Kiko, R. and Deutsch, C.: Global niche of marine anaerobic
945 metabolisms expanded by particle microenvironments, *Nat. Geosci.*, 11(4), 263–268,
946 doi:10.1038/s41561-018-0081-0, 2018.
- 947 Brzezinski, M. A.: A switch from Si(OH)₄ to NO₃⁻ – depletion in the glacial Southern Ocean,
948 *Geophys. Res. Lett.*, 29(12), doi:10.1029/2001gl014349, 2002.
- 949 Cao, L., Eby, M., Ridgwell, A., Caldeira, K., Archer, D., Ishida, A., Joos, F., Matsumoto, K.,
950 Mikolajewicz, U., Mouchet, A., Orr, J. C., Plattner, G.-K., Schlitzer, R., Tokos, K.,
951 Totterdell, I., Tschumi, T., Yamanaka, Y. and Yool, A.: The role of ocean transport in the
952 uptake of anthropogenic CO₂, *Biogeosciences*, 6(3), 375–390, doi:10.5194/bg-6-375-
953 2009, 2009.
- 954 Carr, M. E., Friedrichs, M. A. M., Schmeltz, M., Noguchi Aita, M., Antoine, D., Arrigo, K. R.,

955 Asanuma, I., Aumont, O., Barber, R., Behrenfeld, M., Bidigare, R., Buitenhuis, E. T.,
956 Campbell, J., Ciotti, A., Dierssen, H., Dowell, M., Dunne, J., Esaias, W., Gentili, B., Gregg,
957 W., Groom, S., Hoepffner, N., Ishizaka, J., Kameda, T., Le Quéré, C., Lohrenz, S., Marra, J.,
958 Mélin, F., Moore, K., Morel, A., Reddy, T. E., Ryan, J., Scardi, M., Smyth, T., Turpie, K.,
959 Tilstone, G., Waters, K. and Yamanaka, Y.: A comparison of global estimates of marine
960 primary production from ocean color, *Deep. Res. Part II Top. Stud. Oceanogr.*, 53(5–7),
961 741–770, doi:10.1016/j.dsr2.2006.01.028, 2006.

962 Cheng, H., Edwards, R. L., Southon, J., Matsumoto, K., Feinberg, J. M., Sinha, A., Zhou, W., Li,
963 H., Li, X., Xu, Y., Chen, S., Tan, M., Wang, Q., Wang, Y., Ning, Y., Lawrence Edwards, R.,
964 Southon, J., Matsumoto, K., Feinberg, J. M., Sinha, A., Zhou, W., Li, H., Li, X., Xu, Y., Chen,
965 S., Tan, M., Wang, Q., Wang, Y. and Ning, Y.: Atmospheric $^{14}\text{C}/^{12}\text{C}$ changes during the
966 last glacial period from hulu cave, *Science* (80-.), 362(6420), 1293–1297,
967 doi:10.1126/science.aau0747, 2018.

968 Chien, C. Te, Pahlow, M., Schartau, M. and Oschlies, A.: Optimality-based non-Redfield
969 plankton-ecosystem model (OPEM v1.1) in UVic-ESCM 2.9 - Part 2: Sensitivity analysis
970 and model calibration, *Geosci. Model Dev.*, 13(10), 4691–4712, doi:10.5194/gmd-13-
971 4691-2020, 2020.

972 Claussen, M., Mysak, L., Weaver, A., Crucifix, M., Fichefet, T., Loutre, M. F., Weber, S., Alcamo,
973 J., Alexeev, V., Berger, A., Calov, R., Ganopolski, A., Goosse, H., Lohmann, G., Lunkeit, F.,
974 Mokhov, I., Petoukhov, V., Stone, P. and Wang, Z.: Earth system models of intermediate
975 complexity: Closing the gap in the spectrum of climate system models, *Clim. Dyn.*,
976 18(7), 579–586, doi:10.1007/s00382-001-0200-1, 2002.

977 Codispoti, L. A.: An oceanic fixed nitrogen sink exceeding 400 Tg N a⁻¹ vs the concept of
978 homeostasis in the fixed-nitrogen inventory, *Biogeosciences*, 4(2), 233–253,
979 doi:10.5194/bg-4-233-2007, 2007.

980 Deutsch, C., Sarmiento, J. L., Sigman, D. M., Gruber, N. and Dunne, J. P.: Spatial coupling of
981 nitrogen inputs and losses in the ocean, *Nature*, 445(7124), 163–167,
982 doi:10.1038/nature05392, 2007.

983 DeVries, T. and Weber, T.: The export and fate of organic matter in the ocean: New
984 constraints from combining satellite and oceanographic tracer observations, *Global*
985 *Biogeochem. Cycles*, 31(3), 535–555, doi:10.1002/2016GB005551, 2017.

986 Druffel, E. R. M., Williams, P. M., Bauer, J. E. and Ertel, J. R.: Cycling of dissolved and
987 particulate organic matter in the open ocean, *J. Geophys. Res.*, 97(C10), 15639,
988 doi:10.1029/92JC01511, 1992.

989 Druffel, E. R. M., Griffin, S., Wang, N., Garcia, N. G., McNichol, A. P., Key, R. M. and Walker, B.
990 D.: Dissolved Organic Radiocarbon in the Central Pacific Ocean, *Geophys. Res. Lett.*,
991 46(10), 5396–5403, doi:10.1029/2019GL083149, 2019.

992 Dunne, J. P., Armstrong, R. A., Gnanadesikan, A. and Sarmiento, J. L.: Empirical and
993 mechanistic models for the particle export ratio, *Global Biogeochem. Cycles*, 19(4),
994 n/a-n/a, doi:10.1029/2004GB002390, 2005.

995 Dunne, J. P., Sarmiento, J. L. and Gnanadesikan, A.: A synthesis of global particle export from
996 the surface ocean and cycling through the ocean interior and on the seafloor, *Global*
997 *Biogeochem. Cycles*, 21(4), 1–16, doi:10.1029/2006GB002907, 2007.

998 Eby, M., Weaver, A. J., Alexander, K., Zickfeld, K., Abe-Ouchi, A., Cimadoribus, A. A., Crespin,
999 E., Drijfhout, S. S., Edwards, N. R., Eliseev, A. V., Feulner, G., Fichfet, T., Forest, C. E.,
1000 Goosse, H., Holden, P. B., Joos, F., Kawamiya, M., Kicklighter, D., Kienert, H., Matsumoto,
1001 K., Mokhov, I. I., Monier, E., Olsen, S. M., Pedersen, J. O. P., Perrette, M., Philippon-
1002 Berthier, G., Ridgwell, A., Schlosser, A., Schneider von Deimling, T., Shaffer, G., Smith, R.
1003 S., Spahni, R., Sokolov, A. P., Steinacher, M., Tachiiri, K., Tokos, K., Yoshimori, M., Zeng,
1004 N. and Zhao, F.: Historical and idealized climate model experiments: an
1005 intercomparison of Earth system models of intermediate complexity, *Clim. Past*, 9(3),
1006 1111–1140, doi:10.5194/cp-9-1111-2013, 2013.

1007 Edwards, N. R. and Marsh, R.: Uncertainties due to transport-parameter sensitivity in an
1008 efficient 3-D ocean-climate model, *Clim. Dyn.*, 24(4), 415–433, doi:10.1007/s00382-
1009 004-0508-8, 2005.

1010 Eppley, R. W.: Temperature and phytoplankton growth in the sea, *Fish. Bull.*, 70(4), 1063–
1011 85, 1972.

1012 Galbraith, E. D. and Martiny, A. C.: A simple nutrient-dependence mechanism for predicting
1013 the stoichiometry of marine ecosystems, *Proc. Natl. Acad. Sci.*, 112(27), 8199–8204,
1014 doi:10.1073/pnas.1423917112, 2015.

1015 Garcia, H., Weathers, K. W., Paver, C. R., Smolyar, I., Boyer, T. P., Locarnini, R. A., Zweng, M.
1016 M., Mishonov, A. V., Baranova, O. K., Seidov, D. and Reagan, J. R.: *World Ocean Atlas*

1017 2018. Volume 4: Dissolved Inorganic Nutrients (phosphate, nitrate and nitrate+nitrite,
1018 silicate), NOAA Atlas NESDIS 84, 84(July), 35, 2018.

1019 Garcia, H. E., Weathers, K., Paver, C. R., Smolyar, I., Boyer, T. P., Locarnini, R. A., Zweng, M.
1020 M., Mishonov, A. V., Baranova, O. K., Seidov, D. and Reagan, J. R.: World Ocean Atlas
1021 2018, Volume 3: Dissolved Oxygen, Apparent Oxygen Utilization, and Oxygen
1022 Saturation, NOAA Atlas NESDIS, 3(83), 38 pp., 2019.

1023 Gruber, N. and Sarmiento, J. L.: Global patterns of marine nitrogen fixation and
1024 denitrification, *Global Biogeochem. Cycles*, 11(2), 235–266, doi:10.1029/97GB00077,
1025 1997.

1026 Hansell, D. A.: Recalcitrant Dissolved Organic Carbon Fractions, *Ann. Rev. Mar. Sci.*, 5, 421–
1027 445, doi:10.1146/annurev-marine-120710-100757, 2013.

1028 Hansell, D. A. and Carlson, C. A.: Deep-ocean gradients in the concentration of dissolved
1029 organic carbon, *Nature*, 395(6699), 263–266, doi:10.1038/26200, 1998.

1030 Hansell, D. A., Carlson, C. A., Repeta, D. J. and Schlitzer, R.: Dissolved Organic Matter in the
1031 Ocean: A Controversy stimulates new insights, *Oceanography*, 22(4), 202–211,
1032 doi:https://doi.org/10.5670/oceanog.2009.109, 2009.

1033 Henson, S. A., Sanders, R., Madsen, E., Morris, P. J., Le Moigne, F. and Quartly, G. D.: A
1034 reduced estimate of the strength of the ocean’s biological carbon pump, *Geophys. Res.
1035 Lett.*, 38(4), n/a-n/a, doi:10.1029/2011GL046735, 2011.

1036 Hutchins, D. A. and Bruland, K. W.: Iron-limited growth and Si:N ratios in a costal upwelling
1037 regime, *Nature*, 393(June), 561–564, 1998.

1038 Joos, F., Roth, R., Fuglestedt, J. S., Peters, G. P., Enting, I. G., Von Bloh, W., Brovkin, V., Burke,
1039 E. J., Eby, M., Edwards, N. R., Friedrich, T., Frölicher, T. L., Halloran, P. R., Holden, P. B.,
1040 Jones, C., Kleinen, T., Mackenzie, F. T., Matsumoto, K., Meinshausen, M., Plattner, G. K.,
1041 Reisinger, A., Segschneider, J., Shaffer, G., Steinacher, M., Strassmann, K., Tanaka, K.,
1042 Timmermann, A. and Weaver, A. J.: Carbon dioxide and climate impulse response
1043 functions for the computation of greenhouse gas metrics: A multi-model analysis,
1044 *Atmos. Chem. Phys.*, 13(5), 2793–2825, doi:10.5194/acp-13-2793-2013, 2013.

1045 Kwiatkowski, L., Aumont, O., Bopp, L. and Ciais, P.: The Impact of Variable Phytoplankton
1046 Stoichiometry on Projections of Primary Production, Food Quality, and Carbon Uptake
1047 in the Global Ocean, *Global Biogeochem. Cycles*, 516–528,

1048 doi:10.1002/2017GB005799, 2018.

1049 Kwiatkowski, L., Aumont, O. and Bopp, L.: Consistent trophic amplification of marine
1050 biomass declines under climate change, *Glob. Chang. Biol.*, 25(1), 218–229,
1051 doi:10.1111/gcb.14468, 2019.

1052 Landolfi, A., Kähler, P., Koeve, W. and Oschlies, A.: Global marine N₂ fixation estimates:
1053 From observations to models, *Front. Microbiol.*, 9(SEP), 1–8,
1054 doi:10.3389/fmicb.2018.02112, 2018.

1055 Lang, S. Q., Butterfield, D. A., Lilley, M. D., Paul Johnson, H. and Hedges, J. I.: Dissolved
1056 organic carbon in ridge-axis and ridge-flank hydrothermal systems, *Geochim.
1057 Cosmochim. Acta*, 70(15), 3830–3842, doi:10.1016/j.gca.2006.04.031, 2006.

1058 Laufkötter, C., John, J. G., Stock, C. A. and Dunne, J. P.: Temperature and oxygen dependence
1059 of the remineralization of organic matter, *Global Biogeochem. Cycles*, 31(7), 1038–
1060 1050, doi:10.1002/2017GB005643, 2017.

1061 Laws, E. A., Falkowski, P. G., Smith, W. O., Ducklow, H. W. and McCarthy, J. J.: Temperature
1062 effects on export production in the open ocean, *Global Biogeochem. Cycles*, 14(4),
1063 1231–1246, doi:10.1029/1999GB001229, 2000.

1064 Lee, S. Y., Chiang, J. C. H., Matsumoto, K. and Tokos, K. S.: Southern Ocean wind response to
1065 North Atlantic cooling and the rise in atmospheric CO₂: Modeling perspective and
1066 paleoceanographic implications, *Paleoceanography*, 26, 1–16,
1067 doi:10.1029/2010PA002004, 2011.

1068 Lenton, T. M., Williamson, M. S., Edwards, N. R., Marsh, R., Price, A. R., Ridgwell, A. J.,
1069 Shepherd, J. G. and Cox, S. J.: Millennial timescale carbon cycle and climate change in an
1070 efficient Earth system model, *Clim. Dyn.*, 26(7–8), 687–711, doi:10.1007/s00382-006-
1071 0109-9, 2006.

1072 Letscher, R. T. and Moore, J. K.: Preferential remineralization of dissolved organic
1073 phosphorus and non-Redfield DOM dynamics in the global ocean: Impacts on marine
1074 productivity, nitrogen fixation, and carbon export, *Global Biogeochem. Cycles*, 29(3),
1075 325–340, doi:10.1002/2014GB004904, 2015.

1076 Levitus, S.: Climatological atlas of the world ocean, US Department of Commerce, National
1077 Oceanic and Atmospheric Administration., 1982.

1078 Mahowald, N. M., Muhs, D. R., Levis, S., Rasch, P. J., Yoshioka, M., Zender, C. S. and Luo, C.:

1079 Change in atmospheric mineral aerosols in response to climate: Last glacial period,
1080 preindustrial, modern, and doubled carbon dioxide climates, *J. Geophys. Res. Atmos.*,
1081 111(D10), n/a-n/a, doi:10.1029/2005JD006653, 2006.

1082 Marchal, O., Stocker, T. F. and Joos, F.: A latitude-depth, circulation-biogeochemical ocean
1083 model for palaeoclimate studies. Development and sensitivities, *Tellus, Ser. B Chem.*
1084 *Phys. Meteorol.*, 50B(3), 290–316, doi:10.1034/j.1600-0889.1998.t01-2-00006.x,
1085 1998.

1086 Martiny, A. C., Pham, C. T. A. A., Primeau, F. W., Vrugt, J. A., Moore, J. K., Levin, S. A. and
1087 Lomas, M. W.: Strong latitudinal patterns in the elemental ratios of marine plankton
1088 and organic matter, *Nat. Geosci.*, 6(4), 279–283, doi:10.1038/ngeo1757, 2013.

1089 Mather, R. L., Reynolds, S. E., Wolff, G. A., Williams, R. G., Torres-Valdes, S., Woodward, E. M.
1090 S., Landolfi, A., Pan, X., Sanders, R. and Achterberg, E. P.: Phosphorus cycling in the
1091 North and South Atlantic Ocean subtropical gyres, *Nat. Geosci.*, 1(7), 439–443,
1092 doi:10.1038/ngeo232, 2008.

1093 Matsumoto, K. and Key, R. M.: Natural radiocarbon distribution in the deep ocean, in *Global*
1094 *Environmental Change in the Ocean and on Land*, edited by M. Shiyomi, H. Kawahata,
1095 H. Koizumi, A. Tsuda, and Y. Awaya, pp. 45–58, Terrapub, Tokyo. [online] Available
1096 from: <http://svr4.terrapub.co.jp/e-library/kawahata/pdf/045.pdf>, 2004.

1097 Matsumoto, K. and McNeil, B.: Decoupled response of ocean acidification to variations in
1098 climate sensitivity, *J. Clim.*, 26, 1764–1771, doi:10.1175/JCLI-D-12-00290.1, 2012.

1099 Matsumoto, K. and Tanioka, T.: Shifts in regional production as a driver of future global
1100 ocean production stoichiometry, *Environ. Res. Lett.*, 15(124027), doi:10.1088/1748-
1101 9326/abc4b0, 2020.

1102 Matsumoto, K. and Yokoyama, Y.: Atmospheric $\Delta 14\text{C}$ reduction in simulations of Atlantic
1103 overturning circulation shutdown, *Global Biogeochem. Cycles*, 27(2), 296–304,
1104 doi:10.1002/gbc.20035, 2013.

1105 Matsumoto, K., Tokos, K. S., Price, A. R. and Cox, S. J.: First description of the Minnesota
1106 Earth System Model for Ocean biogeochemistry (MESMO 1.0), *Geosci. Model Dev.*, 1(1),
1107 1–15, doi:10.5194/gmd-1-1-2008, 2008.

1108 Matsumoto, K., Tokos, K., Chikamoto, M. and Ridgwell, A.: Characterizing post-industrial
1109 changes in the ocean carbon cycle in an Earth system model, *Tellus B Chem. Phys.*

1110 Meteorol., 62(4), 296–313, doi:10.1111/j.1600-0889.2010.00461.x, 2010.

1111 Matsumoto, K., Tokos, K., Huston, A. and Joy-Warren, H.: MESMO 2: a mechanistic marine
1112 silica cycle and coupling to a simple terrestrial scheme, *Geosci. Model Dev.*, 6(2), 477–
1113 494, doi:10.5194/gmd-6-477-2013, 2013.

1114 Matsumoto, K., Rickaby, R. and Tanioka, T.: Carbon Export Buffering and CO₂ Drawdown by
1115 Flexible Phytoplankton C:N:P Under Glacial Conditions, *Paleoceanogr.*
1116 *Paleoclimatology*, 35(7), 1–22, doi:10.1029/2019PA003823, 2020.

1117 Moore, J. K., Doney, S. C. and Lindsay, K.: Upper ocean ecosystem dynamics and iron cycling
1118 in a global three-dimensional model, *Global Biogeochem. Cycles*, 18(4), 1–21,
1119 doi:10.1029/2004GB002220, 2004.

1120 Mopper, K., Zhou, X., Kieber, R. J., Kieber, D. J., Sikorski, R. J. and Jones, R. D.: Photochemical
1121 degradation of dissolved organic carbon and its impact on the oceanic carbon cycle,
1122 *Nature*, 353(6339), 60–62, doi:10.1038/353060a0, 1991.

1123 Najjar, R. G., Sarmiento, J. L. and Toggweiler, J. R.: Downward transport and fate of organic
1124 matter in the ocean: Simulations with a general circulation model, *Global Biogeochem.*
1125 *Cycles*, 6(1), 45–76, doi:10.1029/91GB02718, 1992.

1126 Pahlow, M. and Oschlies, A.: Chain model of phytoplankton P, N and light colimitation, *Mar.*
1127 *Ecol. Prog. Ser.*, 376(2), 69–83, doi:10.3354/meps07748, 2009.

1128 Pahlow, M. and Oschlies, A.: Optimal allocation backs droop’s cell-quota model, *Mar. Ecol.*
1129 *Prog. Ser.*, 473(2010), 1–5, doi:10.3354/meps10181, 2013.

1130 Pahlow, M., Dietze, H. and Oschlies, A.: Optimality-based model of phytoplankton growth
1131 and diazotrophy, *Mar. Ecol. Prog. Ser.*, 489, 1–16, doi:10.3354/meps10449, 2013.

1132 Pahlow, M., Chien, C. Te, Arteaga, L. A. and Oschlies, A.: Optimality-based non-Redfield
1133 plankton-ecosystem model (OPEM v1.1) in UVic-ESCM 2.9 - Part 1: Implementation
1134 and model behaviour, *Geosci. Model Dev.*, 13(10), 4663–4690, doi:10.5194/gmd-13-
1135 4663-2020, 2020.

1136 Paulsen, H., Ilyina, T., Six, K. D. and Stemmler, I.: Incorporating a prognostic representation
1137 of marine nitrogen fixers into the global ocean biogeochemical model HAMOCC, *J. Adv.*
1138 *Model. Earth Syst.*, 9(1), 438–464, doi:10.1002/2016MS000737, 2017.

1139 Ridgwell, A.: Glacial-interglacial perturbations in the global carbon cycle, Ph. D. thesis, 134
1140 pp., Univ. East Anglia, Norwich, U. K. Ridgwell, A. J., U. Edwards, 2001.

1141 Ridgwell, A., Hargreaves, J. C., Edwards, N. R., Annan, J. D., Lenton, T. M., Marsh, R., Yool, A.
1142 and Watson, A.: Marine geochemical data assimilation in an efficient Earth System
1143 Model of global biogeochemical cycling, *Biogeosciences*, 4(4), 87–104, doi:10.5194/bg-
1144 4-87-2007, 2007.

1145 Ridgwell, A. J., Watson, A. J. and Archer, D. E.: Modeling the response of the oceanic Si
1146 inventory to perturbation, and consequences for atmospheric CO₂, *Global*
1147 *Biogeochem. Cycles*, 16(4), 19-1-19–25, doi:10.1029/2002GB001877, 2002.

1148 Roshan, S. and DeVries, T.: Efficient dissolved organic carbon production and export in the
1149 oligotrophic ocean, *Nat. Commun.*, 8(1), 2036, doi:10.1038/s41467-017-02227-3,
1150 2017.

1151 Sarmiento, J. L., Gruber, N., Brzezinski, M. A. and Dunne, J. P.: High-latitude controls of
1152 thermocline nutrients and low latitude biological productivity, *Nature*, 427(6969), 56–
1153 60, doi:10.1038/nature02127, 2004.

1154 Sun, X. and Matsumoto, K.: Effects of sea ice on atmospheric p CO₂ : A revised view and
1155 implications for glacial and future climates, *J. Geophys. Res.*, 115(G02015),
1156 doi:10.1029/2009JG001023, 2010.

1157 Sunda, W. G. and Huntsman, S. A.: Iron uptake and growth limitation in oceanic and coastal
1158 phytoplankton, *Mar. Chem.*, 50(1–4), 189–206, doi:10.1016/0304-4203(95)00035-P,
1159 1995.

1160 Sverdrup, H. U.: On the conditions for the vernal blooming of phytoplankton, *J. Cons. Perm.*
1161 *Int. Pour l'Exploration La Mer*, 18, 287–195, 1953.

1162 Takeda, S.: Influence of iron availability on nutrient consumption ratio, *Nature*, 393(JUNE),
1163 774–777, 1998.

1164 Tanioka, T. and Matsumoto, K.: Buffering of Ocean Export Production by Flexible Elemental
1165 Stoichiometry of Particulate Organic Matter, *Global Biogeochem. Cycles*, 31(10), 1528–
1166 1542, doi:10.1002/2017GB005670, 2017.

1167 Tanioka, T. and Matsumoto, K.: A meta-analysis on environmental drivers of marine
1168 phytoplankton C : N : P, *Biogeosciences*, 17(11), 2939–2954, doi:10.5194/bg-17-2939-
1169 2020, 2020a.

1170 Tanioka, T. and Matsumoto, K.: Stability of Marine Organic Matter Respiration
1171 Stoichiometry, *Geophys. Res. Lett.*, 47(1), 1–10, doi:10.1029/2019GL085564, 2020b.

1172 Ushie, H. and Matsumoto, K.: The role of shelf nutrients on glacial-interglacial CO₂: A
1173 negative feedback, *Global Biogeochem. Cycles*, 26, 1–10, doi:10.1029/2011GB004147,
1174 2012.

1175 Wang, W.-L., Moore, J. K., Martiny, A. C. and Primeau, F. W.: Convergent estimates of marine
1176 nitrogen fixation, *Nature*, 566(7743), 205–211, doi:10.1038/s41586-019-0911-2,
1177 2019.

1178 Wanninkhof, R.: Relationship between wind speed and gas exchange over the ocean, *J.*
1179 *Geophys. Res.*, 97(C5), 7373–7382, doi:10.1029/92JC00188, 1992.

1180 Weaver, A. J., Sedlá, J., Eby, M., Alexander, K., Crespin, E., Fichfet, T., Philippon-berthier, G.,
1181 Joos, F., Kawamiya, M., Matsumoto, K., Steinacher, M., Tachiiri, K., Tokos, K., Yoshimori,
1182 M. and Zickfeld, K.: Stability of the Atlantic meridional overturning circulation : A
1183 model intercomparison, *Geophys. Res. Lett.*, 39, 1–7, doi:10.1029/2012GL053763,
1184 2012.

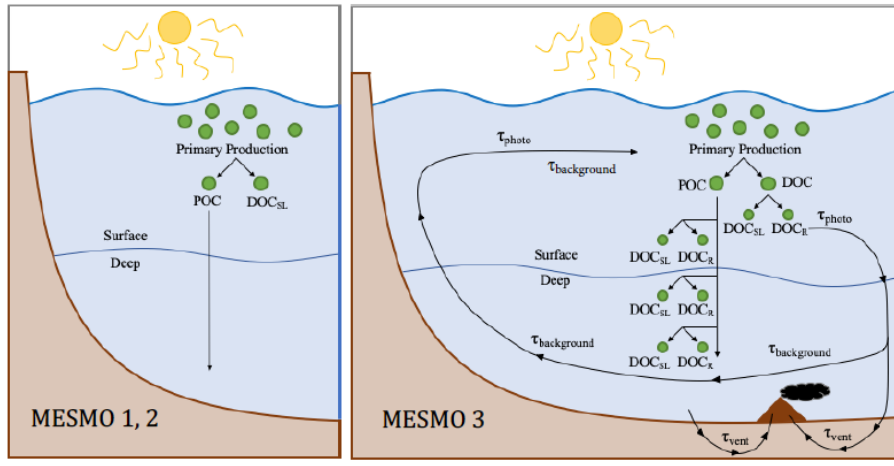
1185 Yamanaka, Y. and Tajika, E.: Role of dissolved organic matter in the marine biogeochemical
1186 cycle: Studies using an ocean biogeochemical general circulation model, *Global*
1187 *Biogeochem. Cycles*, 11(4), 599–612, doi:10.1029/97GB02301, 1997.

1188 Yamanaka, Y., Yoshie, N., Fujii, M., Aita, M. N. and Kishi, M. J.: An Ecosystem Model Coupled
1189 with Nitrogen-Silicon-Carbon Cycles Applied to Station A7 in the Northwestern Pacific,
1190 *J. Oceanogr.*, 60(2), 227–241, doi:10.1023/B:JOCE.0000038329.91976.7d, 2004.

1191 Zickfeld, K., Eby, M., Weaver, A. J., Alexander, K., Crespin, E., Edwards, N. R., Eliseev, A. V.,
1192 Feulner, G., Fichfet, T., Forest, C. E., Friedlingstein, P., Goosse, H., Holden, P. B., Joos, F.,
1193 Kawamiya, M., Kicklighter, D., Kienert, H., Matsumoto, K., Mokhov, I. I., Monier, E.,
1194 Olsen, S. M., Pedersen, J. O. P., Perrette, M., Philippon-Berthier, G., Ridgwell, A.,
1195 Schlosser, A., Von Deimling, T. S., Shaffer, G., Sokolov, A., Spahni, R., Steinacher, M.,
1196 Tachiiri, K., Tokos, K. S., Yoshimori, M., Zeng, N. and Zhao, F.: Long-Term climate
1197 change commitment and reversibility: An EMIC intercomparison, *J. Clim.*, 26(16),
1198 5782–5809, doi:10.1175/JCLI-D-12-00584.1, 2013.

1199
1200

1201

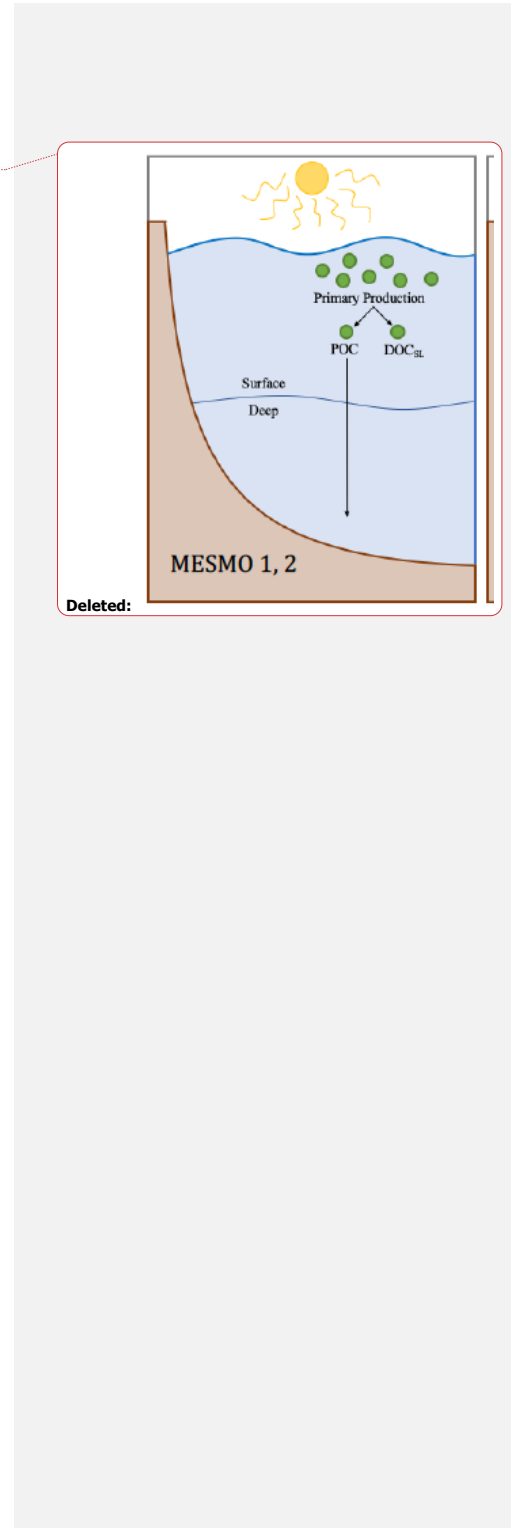


1202

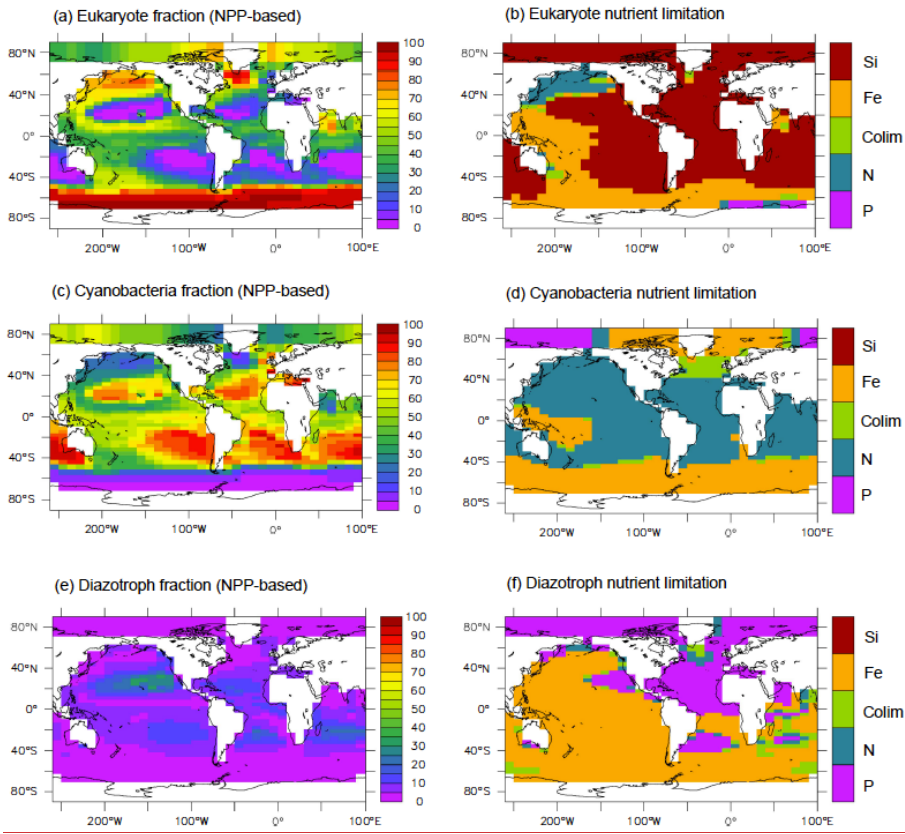
1203 **Figure 1.** Schematic diagram of DOM cycling in MESMO 2 versus MESMO 3. In the new
 1204 model, DOM_r can be activated. DOM_r is produced from POM breakdown, which can occur in
 1205 the production layer or throughout the water column in the "deep POC split." Possible
 1206 DOM_r remineralization mechanisms are the slow background degradation that occurs
 1207 everywhere, thermal degradation in hydrothermal vents, and photodegradation in the
 1208 surface. See text for details.

1209

1210



1212

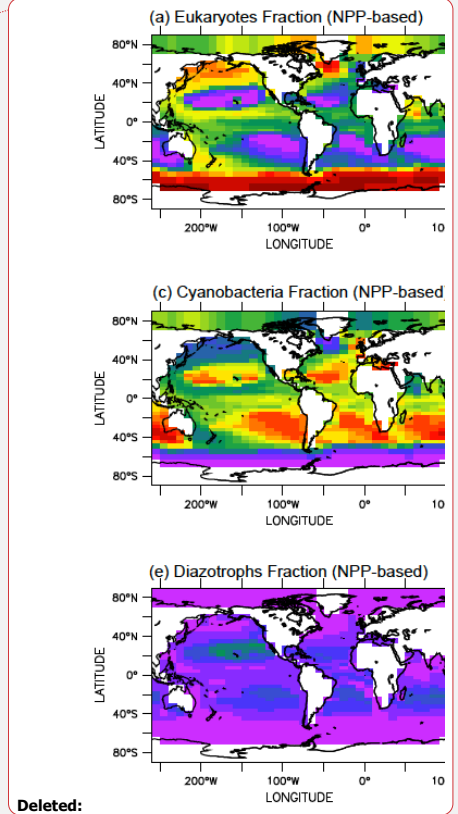


1213

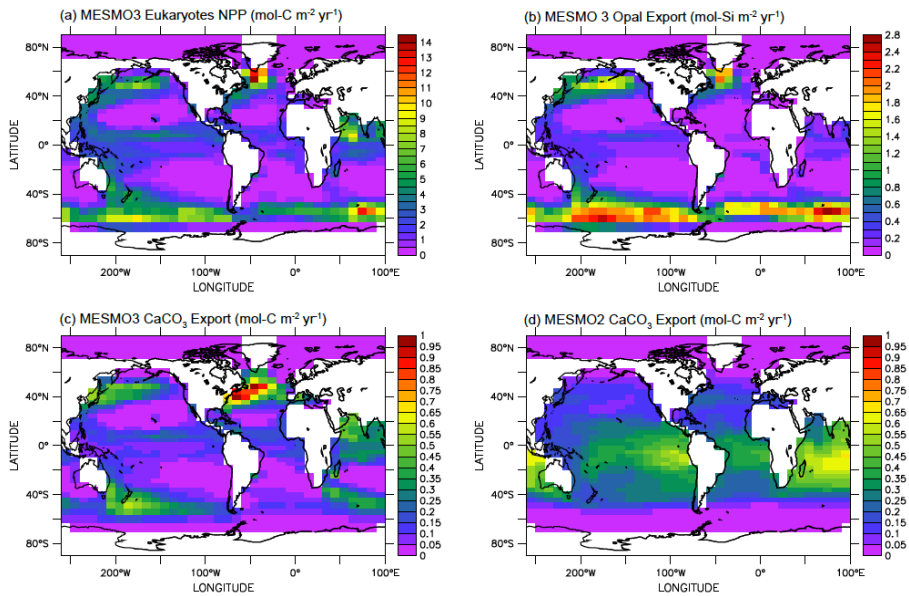
1214 **Figure 2.** NPP-based surface phytoplankton functional type (PFT) abundance and nutrient
 1215 limitation in MESMO 3. Fractional abundance and nutrient limitation for eukaryotes (a, b),
 1216 cyanobacteria (c, d), and diazotrophs (e, f).

1217

1218



Deleted:



1220

1221

1222

1223

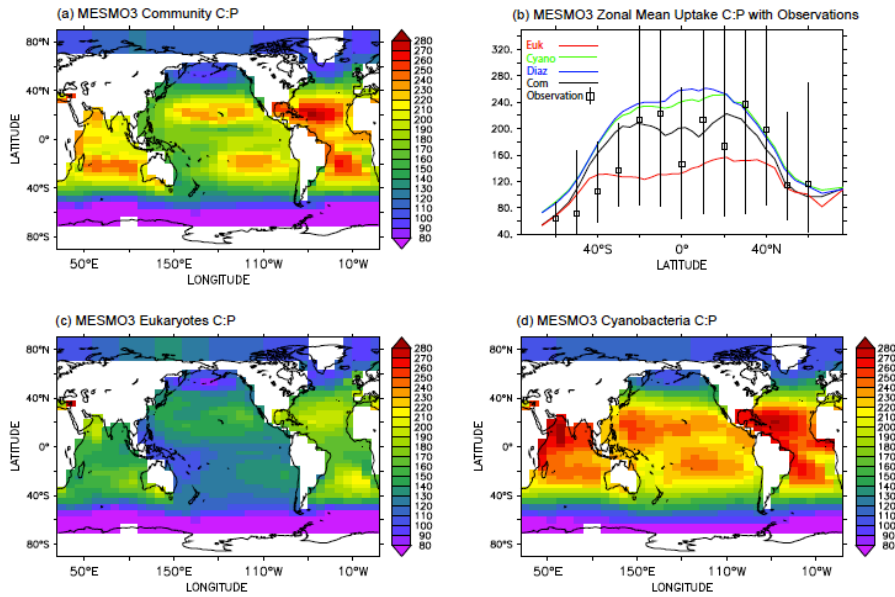
1224

1225

Figure 3. Eukaryote production in MESMO 3 and CaCO₃ export in MESMO 2. In MESMO 3, eukaryote NPP (a) is linked to both opal export (b) and CaCO₃ export (c) but the two export productions are differentiated by the residual nitrate potential growth (RNPG). Compare CaCO₃ export in MESMO 3 (c) to MESMO 2 (d). Unit = mol m⁻² year⁻¹.

Deleted: The effect of the residual nitrate potential growth (RNPG) on the eukaryote production in MESMO 3. Eukaryote NPP (a), opal export (b), and CaCO₃ export (c) in MESMO 3. CaCO₃ export in MESMO 2 (d). Unit = mol m⁻² year⁻¹.

1230

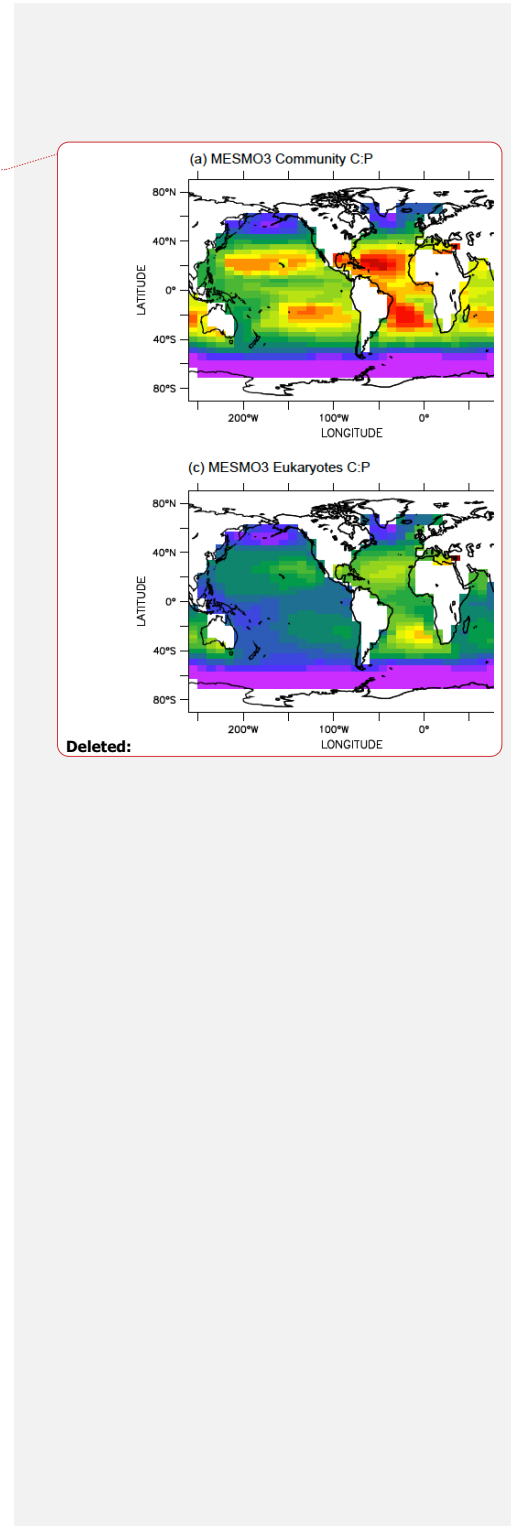


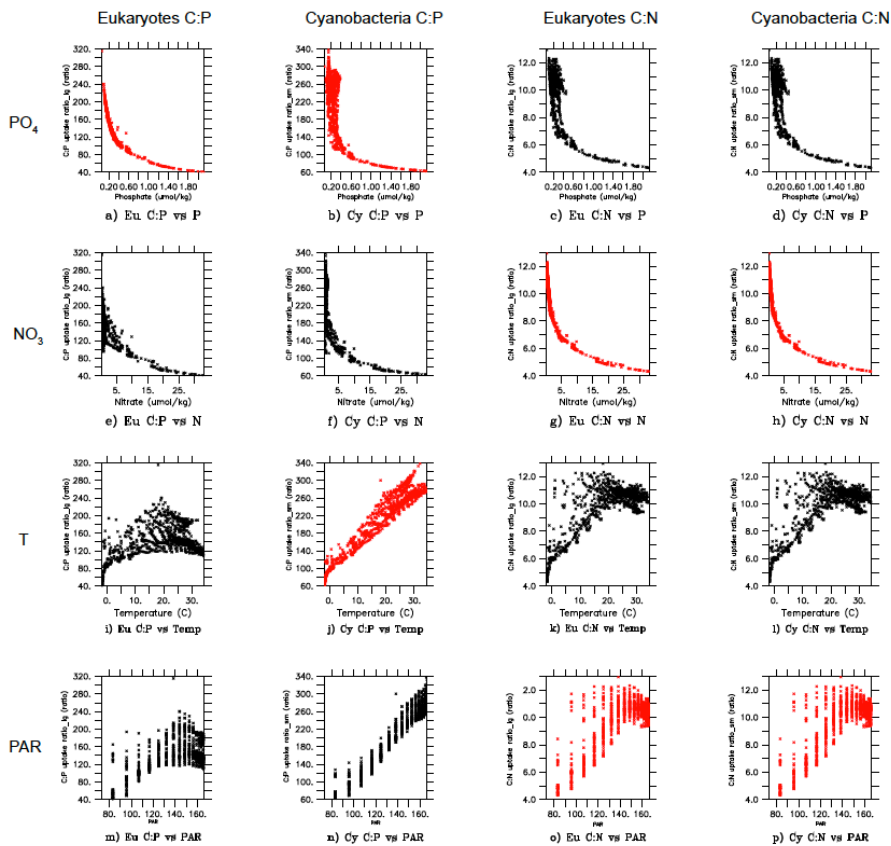
1231

1232 **Figure 4.** Uptake C:P ratio in the top 100 m in MESMO 3: (a) phytoplankton community C:P,
 1233 (b) zonal mean C:P of all three PFTs and phytoplankton community, (c) eukaryote C:P, and
 1234 (d) cyanobacteria C:P. The colors in (b) indicate: black = community C:P, red = eukaryote
 1235 C:P, green = cyanobacteria C:P, and blue = diazotroph C:P. *Also, (b) shows the range of*
 1236 *observed C:P ratio binned by latitude (Martiny et al., 2013).*

1237

1238





1240

1241 **Figure 5.** Scatter plots of surface ocean eukaryote and cyanobacteria C:P and C:N vs.

1242 environmental drivers in MESMO 3. Columns: 1 = eukaryote C:P, 2 = cyanobacteria C:P, 3 =

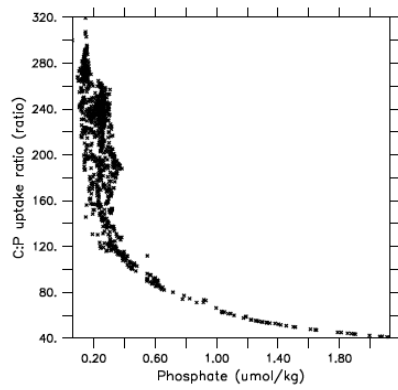
1243 eukaryote C:N, and 4 = cyanobacteria C:N. Rows: 1 = PO₄, 2 = NO₃, 3 = temperature, and 4 =

1244 PAR. Red indicates causal relationship according to the power law formulation of flexible

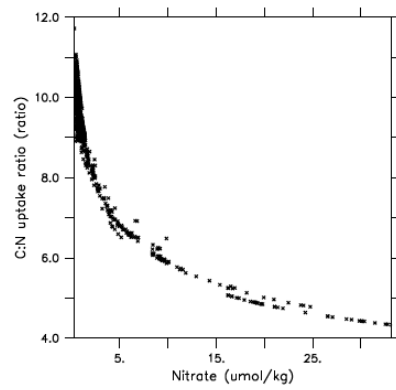
1245 C:N:P ratio. PAR = photosynthetically active radiation in W m⁻².

1246

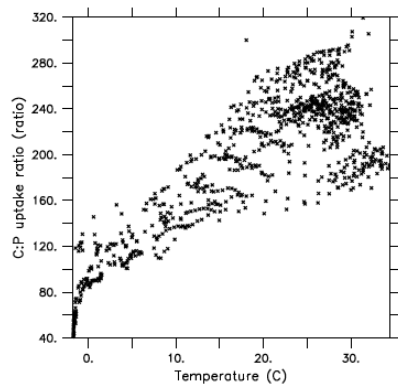
1247



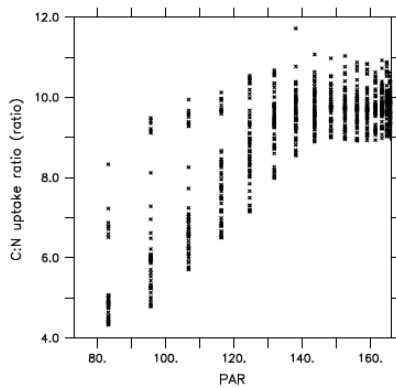
com C:P vs P



com C:N vs N



com C:P vs Temp



com C:N vs PAR

1248

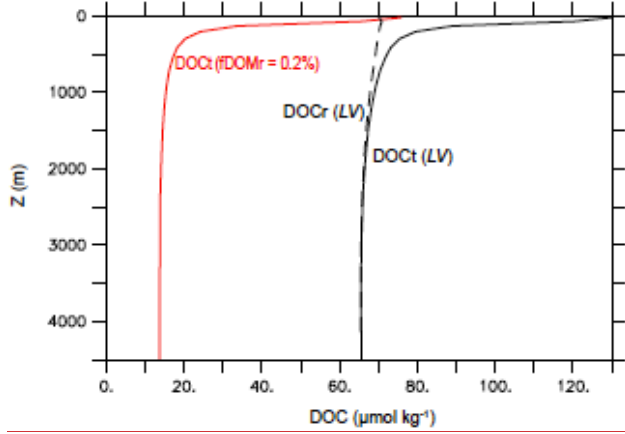
1249 **Figure 6.** Scatter plots of surface ocean community C:P and C:N vs environmental drivers in

1250 MESMO 3.

1251

1252

1253



1254

1255

1256

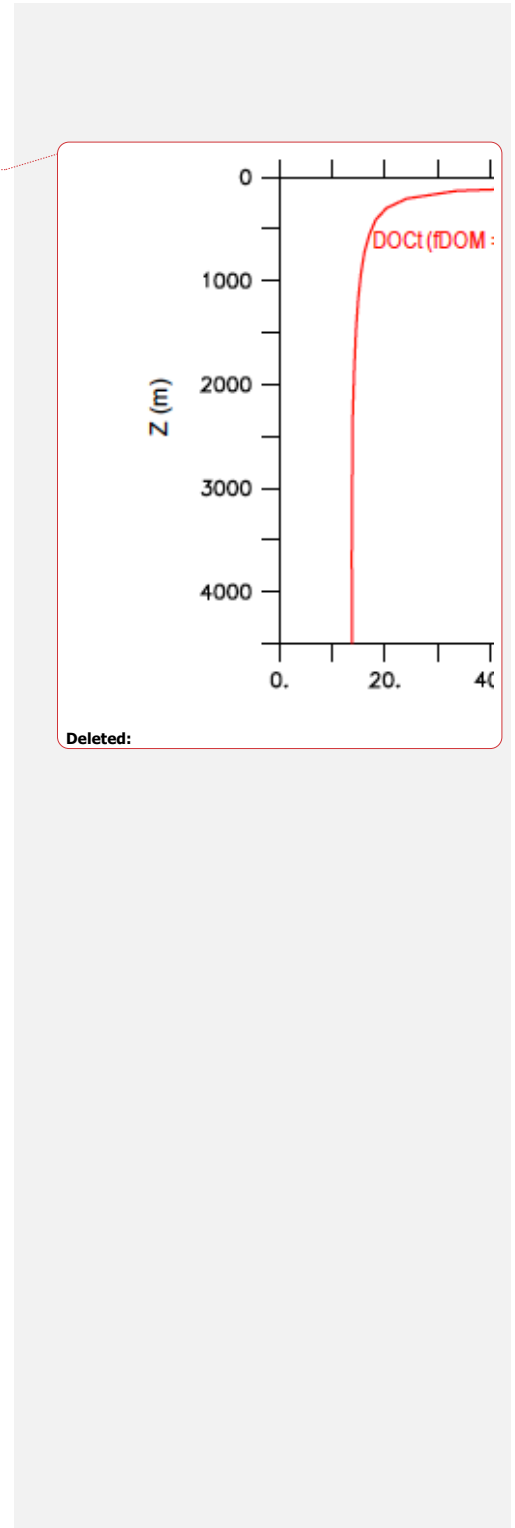
1257

1258

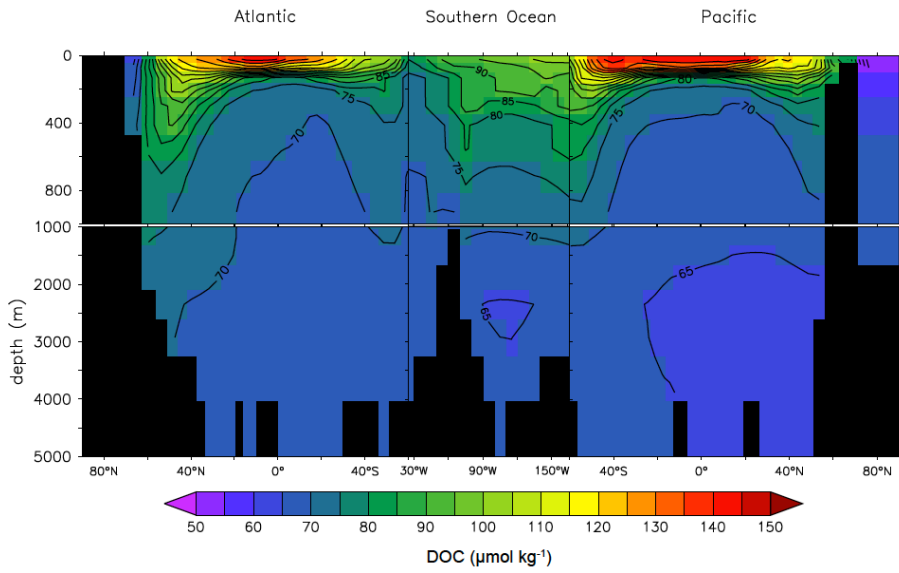
1259

Figure 7. Global mean

vertical profiles of DOC from the DOM_R-enabled MESMO 3. DOC_t (DOC_s+DOC_r, black line) and DOC_r (black dashed line) from the LV run (Experiment 210310m). Red line is DOC_t after reducing fDOM_r from 1% in LV to 0.2% (Experiment 210310o). Unit = μmol kg⁻¹.



Deleted:



1261

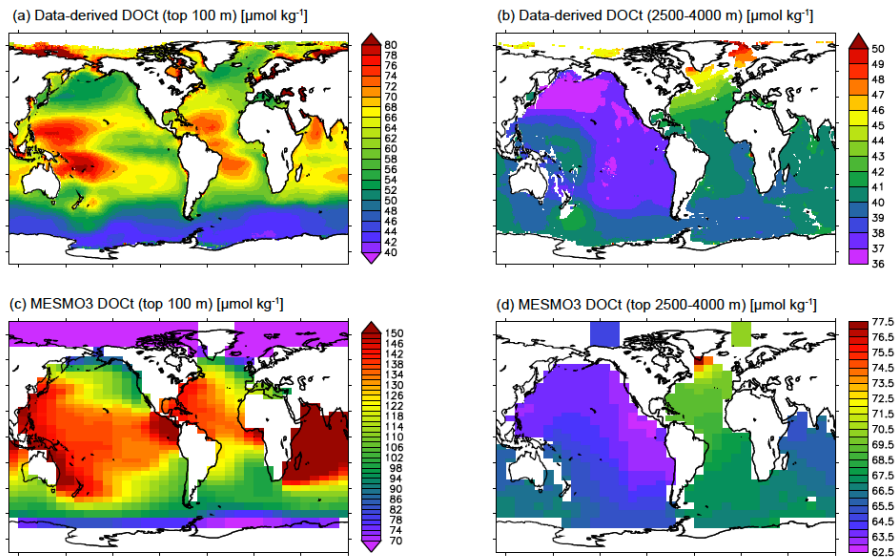
1262 **Figure 8.** Global depth-latitude transect of DOC_t from the DOM_R -enabled MESMO 3 LV run.

1263 Transects are N-S along 25°W in the Atlantic, E-W along 60°S in the Southern Ocean, and N-

1264 S along 165°E in the Pacific. Unit = $\mu\text{mol kg}^{-1}$.

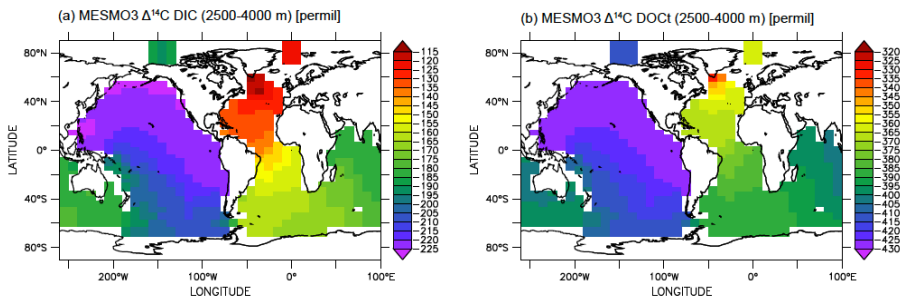
1265

1266



1267
 1268 **Figure 9.** Assessment of surface and deep ocean DOC_t from the DOM_R -enabled MESMO 3 *LV*
 1269 run. Data-derived DOC_t distributions in the top 100 m (a) and 2500-4000 m (b). Model-
 1270 simulated DOC_t distributions in the top 100 m (c) and 2500-4000 m (d). Date-derived DOC_t
 1271 are from Roshan and DeVries (Roshan and DeVries, 2017). Unit = $\mu\text{mol kg}^{-1}$.

1272
 1273



1274

1275 **Figure 10.** $\Delta^{14}\text{C}$ of deep ocean DIC (a) and DOC_t (b) from the DOM_R -enabled MESMO 3 LV

1276 run. Vertical average over 2500-4000 m water depth. Unit = ‰.

1277

1278